Real-Time Interrogation of Optical Sensors Based on Wavelength-to-Time Mapping

Hong Deng

Thesis submitted in partial fulfillment of the requirements for the Master of Applied Science degree in Electrical and Computer Engineering

School of Electrical Engineering and Computer Science

Faculty of Engineering

University of Ottawa

uOttawa

ACKNOWLEDGEMENTS

First, I would like to express my sincere gratitude to my supervisor, Prof. Jianping Yao, for providing a strong but free academic atmosphere, state-of-the-art research equipment and considerate guidance. I have been deeply touched by his dedication and passion for research. The door to Prof. Yao office was always open whenever I had a question about my research. Without his support, I would never complete these research work.

I am grateful to my colleagues, Dr. Jiejun Zhang, who patiently and thoughtfully coached me the experimental skills and the FBG fabrication processes; Dr. Weifeng Zhang, who thoroughly introduced me the principles of chip design and chip test; Prof. Zhiyao Zhang, whose suggestions helped me complete this work.

I would like to sincerely thank all my other colleagues in the Microwave Photonics Research Laboratory at the University of Ottawa for providing a friendly and supportive environment. They are Dr. Xiang Chen, Dr. Weilin Liu, Jishen Li, Dr. Ou Xu and Prof. Yishi Han.

I would like to thank Prof. Lukas Chrostowski, for guiding me into the world of silicon photonics via the Si-EPIC workshops. I would like to thank Prof. Ping Lu, for providing the random gratings used in my experiments. I would also like to thank Dr. Jessica Zhang and Dr. Dan Deptuck in the CMC Microsystems, for providing the design tools and for their support in the design and fabrication of the silicon photonic devices.

Finally, I appreciate the love and support from my girlfriend and my family. It is their love that supports me going further in the pursuit of knowledge.

ABSTRACT

Theoretical and experimental studies of real-time interrogation of optical sensors based on wavelength-to-time (WTT) mapping are presented. The sensing information is encoded in the spectrum of an optical sensor, and transferred to the time domain by using WTT mapping. Utilizing digital electronics for post processing, the sensing information can be interrogated at an ultra-high speed and resolution. Two sensors based on WTT mapping are proposed and demonstrated.

First, a random grating sensor for simultaneous measurement of the temperature and strain is investigated. An ultra-short pulse from a mode-lock laser is spectrum shaped by a high-birefringence random grating to generate two orthogonally polarized spectrums, which are then fed to an optical loop in which a linearly chirped fiber Bragg grating is incorporated. Linear WTT mapping is implemented, and two temporally separated optical pulses are generated, and then converted to two electrical waveforms at a photodetector. Pulse compression is then employed. By measuring the temporal intervals of the temporally compressed pulses, the strain and temperature information can be retrieved.

Conventional fiber based sensors are not sensitive to the refractive index change of the environment. In the second sensor, a silicon photonic microdisk resonator (MDR) for temperature and liquid refractive index sensing is proposed and demonstrated. By using the notches in the spectrum of the MDR, a microwave photonic filter (MPF) is implemented. By feeding a linearly chirped microwave signal to the MPF, a filtered signal with its temporal

location representing the spectrum is generated. By monitoring the time location of the filtered signal, the temperature or the refractive index information is revealed.

TABLE OF CONTENTS

LIST OF FIGURES

LIST OF ACRONYMS

ASE	Amplified spontaneous emission
AWG	Arbitrary waveform generation
CMOS	Complementary metal oxide silicon
CTE	Coefficient of thermal expansion
DCF	Dispersion compensating fiber
EA	Electrical amplifier
EC	Electrical coupler
EDFA	Erbium doped fiber amplifier
EOM	Electro-optic modulator
FSR	Free spectral range
FBG	Fiber Bragg grating
HBRG	High-birefringence random grating
LCFBG	Linearly chirped fiber Bragg grating
LCMW	Linearly chirped microwave waveform
LD	Laser diode
LPG	Long period grating
MDR	Microdisk resonator
MLL	Mode-locked laser
MPF	Microwave photonic filter
MRR	Micro-ring resonator
MZI	Mach-Zehnder interferometer

OADM	optical add-drop multiplexer
OC	Optical circulator
OEO	Opto-electronic oscillator
OSA	Optical spectrum analyzer
OVA	Optical vector analyzer
PBS	Polarization beam splitter
PC	Polarization controller
PD	Photodetector
POF	Phase-only filter
PS-FBG	Phase-shifted fiber Bragg grating
SMF	Single mode fiber
SNR	Signal-to-noise ratio
SS	Spectral-shaping
TBWP	Time-bandwidth product
TLS	Tunable laser source
UV	Ultraviolet
WTT	Wavelength-to-time

CHAPTER 1 INTRODUCTION

1.1 Background Review

Optical sensing, based on fiber or other technologies, plays an important role in numerous applications, for its intrinsic advantages, such as no physic contact, immunity to electromagnetic interference, high sensitivity, light weight, small size, environmental ruggedness, multiplexing and distributed capacities [1]. In oil and gas industry, optical sensors help engineers monitor the pressure and temperatures of wells without the risk of explosion [2]. In the aviation industry, Airbus is investigating using optical fiber sensors in their A380 airplanes, to measure the actual loads experienced by the structures without having any adverse impact on the mechanical properties of the structure [3]. In the civil applications, optical fiber sensors are used to detect the pipeline buckling [4], wall-thinning defects [5] or pipeline leaks [6]. Optical biosensors are also attractive in medical applications [7]. Fiber pH sensors [8] and fiber oxygen sensors [9] have been reported, and even the DNA hybridization can be directly analyzed by using an optical fiber sensor [10]. To data, more than 70 different parameters can be detected by using optical fiber sensors, such as temperature, pressure, strain, acceleration, vibration and so on. With price getting lower and quality getting higher, the capability of optical sensors will be enhanced further.

Various optical sensors have been designed and realized in the last 40 years. Most of the optical sensors are based on optical fibers. Using an interferometric system for the measurement can build an interferometric sensor with an ultrahigh sensitivity [11], [12], while the cross-sensitivity problems often arise when the impact of other parameters, or noises, cannot be suppressed or calibrated. Taking advantage of the linear and non-linear effects in the fiber, such

as Rayleigh backscattering [13], Raman scattering [14], Brillouin scattering [15], and Kerr effect [16], in an optical fiber, distributed fiber sensors can be realized, with a high spatial resolution and a high sensitivity. However, due to the low non-linear coefficients of silica, the energy of an optical sensing signal is very low, leading to a long response time to integrate a small signal received over many pulses. Fiber gratings, such as fiber Bragg gratings (FBGs) [17], long period gratings (LPGs) [18], and random gratings [19] are also proved to be useful as fiber sensors for the detection of vibration and strains, with all the advantages attributed to fiber sensors [20]. By encoding the sensing parameters directly into wavelength, the influence of the light intensity or losses are muted. However, grating sensors show a high temperature dependence, while the temperature compensation mostly requires special arrangements and an FBG sensor as a reference sensor. Grating sensors also sensitive to pressures causing light birefringence, which causes two separate reflection pulses, leading to an ambiguous interrogation.

On the other hand, all these fiber-based structures are based on bulk components, which limits the practicality in point of care testing and other medical biosensing applications, and the basic pure fiber is not sensitive to the refractive index change of the environment [21]. Integrated optical sensors, with a high sensitivity to the refractive index change, have been studied for over 20 years. As the same as the optical fiber sensors, integrated optical sensors based on interferences [22] [23] [24], Raman scattering [25], Brillouin scattering [26], and resonances [27] [28] have been proposed and experimentally implemented.

In order to further reduce the cost in fabrication, silicon photonics, with the compatibility of the current CMOS technology and the potential for seamless integration with electronics, is becoming attractive for the fabrication of optical devices with large-scale integration at a

reasonable cost. Due to the intrinsic feature of silicon, such as low absorption and low non-linear coefficients at the commonly used wavelength band, silicon photonic sensors are mainly based on the waveguide resonators. In the past few years, silicon photonic resonator sensors, such as waveguide Bragg gratings (WBGs) [29], phase shifted Bragg gratings [30], microring resonators (MRRs) [31] and microdisk resonators (MDRs) [32] have been proposed and developed using different materials and for different sensing applications. Compared with a basic straight waveguide, whose interaction is determined by the physical length, the interaction of the environment and the light field in a resonator is multiplicated by the number of roundtrips by the light inside the cavity, leading to a high detection sensitivity [33]. The number of roundtrips can be described by the quality factor (Q factor) of the resonator. Therefore, a resonator with a higher Q factor is always needed to get a higher sensitivity.

For an optical resonator based sensor, the sensing parameters are encoded in the resonant wavelengths. For interrogating or demodulating the sensing information, a straightforward method is to use an optical spectrum analyzer (OSA) to monitor the resonant wavelength shifts. However, a commonly used OSA could only provide a wavelength resolution of 20 pm (YOKOGAWA, AQ6370D), while the 3-dB bandwidth of a silicon photonic microring resonator with a typical Q factor of 40000 is around 38.75 pm, and the 3-dB bandwidth of a typical phase-shifted FBG (PS-FBG) is about 0.24 pm, which are close to or lower than the wavelength resolution of an OSA. Thus, the interrogation resolution of the approaches using an OSA is very limited. An alternative method is to use a tunable laser source (TLS) and an optical power meter. The wavelength resolution can be improved to around 1 pm (Keysight 81606A), but the tuning speed is still very low.

To increase the interrogation speed and interrogation resolution, diverse techniques have been proposed. For example, using a bulky dispersive element to convert the wavelength information to its spatial light distribution and using a linear-array detector to detect the spatial light distribution, the wavelength information can be measured in real time [34]. Although the system in [34] is simple and stable, the free-space implementation makes the system relatively bulky. The use of an optical edge filter to convert the wavelength information to an intensity change is another approach which can provide real time interrogation [35] [36]. The major limitation of using an edge filter is the power variations from the light source, which would be translated to intensity change, making the interrogation accuracy reduced. To increase the accuracy, optical interferometer scanners can be used to convert the wavelength shift to a change in optical phase, and the phase shift is estimated by a lock-in amplifier [37]. The measurement resolution is significantly improved, but the stability is poor due to the use of an interferometer which is extremely sensitive to environmental changes.

Recently, optical sensors interrogated based on microwave photonics (MWP) techniques have been proposed. The key advantage of optical sensors using MWP techniques is the ultra-high interrogation speed and resolution, which is realized by translating the wavelength shift in the optical domain to the microwave frequency change in the electrical domain. The microwave frequency change can be measured using digital electronics with an ultra-high speed and resolution. For example, in [38], two FBGs with one serving as a sensor and the other as a reference are used to slice the spectrum of an ultrashort pulse, to generate two spectrums. By using dispersive elements to stretch the light pulse, the two spectrums are converted to the time domain, and two light pulses are generated. By beating the two optical pulses at a photodetector (PD), a temporal interference pattern is generated [39]. The sensing information is obtained by measuring the

frequency of the temporal interference pattern, with an improved interrogation resolution. In [40], an optical chirped pulse is sent two chirped FBGs, with one as a sensor and the other as a reference. Two time-delayed optical chirped pulses are obtained. By beating the two optical pulses at a PD, a de-chirped microwave signal with its frequency corresponding to the time delay difference between the two optical pulses is generated. Since the time delay difference is temperature or strain dependent, the frequency information reveals the sensing information. High precision interrogation can also be done by using an optoelectronic oscillator (OEO) [41]. For example, by using a PS-FBG in an OEO, a microwave signal with its frequency corresponding to the wavelength difference between the optical carrier wavelength and the notch wavelength can be generated. By monitoring the microwave frequency change, high speed and ultra-high resolution interrogation can be achieved. However, the interrogation speed is based on the frequency scanning speed of the spectrum analyser, which is still limited.

To further increase the measurement speed and resolution, wavelength-to-time (WTT) mapping or time stretching technique can be used. A linearly chirped microwave waveform is generated and used in an interrogation system [42]. By performing pulse compression in the time domain, the interrogation speed and resolution can be significantly increased. A similar approach using pulse compression was recently reported in [43], where a linearly chirped microwave waveform was filtered by a microwave photonic filter (MPF) implemented using a PS-FBG. Again, by using pulse compression, the sensing resolution was improved. However, since interferometric structures are employed in these systems, the stability of the systems is poor.

Apart from FBG sensors, a silicon photonic microring sensor based on an OEO was recently proposed, which provided a high detection sensitivity and measurement resolution [44]. However,

because of a large 3-dB bandwidth of the MRR, the OEO loop must be very short and the gain in the loop must be controlled very carefully, to avoid mode hopping. Furthermore, the proposed OEO sensor are not suitable for biosensing, since the 3-dB bandwidth of the microring would broaden significantly when the waveguides are cladded by water or blood.

In this thesis, we propose two real-time interrogation systems for optical sensors based on WTT mapping with improved interrogation speed, resolution and stability.

The first interrogation system is for random grating sensors for measuring the strain and temperature. The key component is a high-birefringence random grating (HBRG) sensor, which is fabricated in a polarization maintaining fiber (PMF) by pseudo-randomly varying the grating periods, providing a random reflection response. An ultra-short pulse from a mode-lock laser (MLL) is spectrum shaped by the HBRG to generate two random spectrums with the wavelength spacing determined by the birefringence of the HBRG, which are then fed to an optical loop in which a linearly chirped fiber Bragg grating (LCFBG) is incorporated. Linear WTT mapping is implemented at the LCFBG in a complementary manner to generate two temporally separated random waveforms, corresponding to the spectrums along two orthogonal polarization directions. Using pulse compression, the temporal shifts of the two random waveforms can be precisely measured, and thus the stain and temperature information can be retrieved. Because of the high randomness of the reflection spectral response of the HBRG, the compressed pulses are very narrow, leading to a high interrogation resolution. Furthermore, using the LCFBG in a complementary manner can provide complementary optical dispersion to the two orthogonally polarized spectrums. Thus, the two WTT mapped temporal waveforms would experience positive and negative time delays, which would make the two temporal waveforms shift in the opposite

directions. The complimentary dispersion coefficients help the two WTT mapped waveform different with each other, avoiding the ambiguity in the interrogation. In addition, without using an interferometric structure, the system is ultra-stable. A theoretical model is developed, which is validated by an experiment in Chapter 3.

The second real time interrogation system is based on a silicon photonic MDR sensor for the measurement of temperature and liquid refractive index. In the proposed system, the MDR is incorporated into a MPF consisting of a laser source, a phase modulator (PM), the MDR, and a PD, with the central frequency of the MPF being a function of the resonant wavelength of the MDR. A broadband linearly chirped microwave waveform (LCMW) is applied to the input of the MPF to generate a filtered microwave waveform. By measuring the temporal location of the filtered microwave waveform, the sensing information is revealed. The interrogation resolution is determined by the bandwidth of the MDR. In the design, to get a high Q factor, the MDR is designed by adding a slab waveguide surrounding the disk and the bus waveguide, then the interaction between the light field and the sidewalls of the disk is weakened, thus the loss due to scattering resulted from sidewall roughness is suppressed and a higher Q factor is archived, which leads to an improved sensing sensitivity and interrogation resolution. The central frequency of the MPF is a function of the resonant wavelength of the MDR, which is sensitive to the change of the temperature or the cladding refractive index. To improve the signal-to-noise ratio (SNR) of the filtered microwave waveform, the microwave waveform is first compressed by correlating it with a phase-only filter (POF) built from the LCMW, which is a reference waveform. Then, a Hamming window is applied to the compressed pulse to remove the noise. By re-correlating the compressed waveform with the POF, a noise-removed microwave waveform is obtained, which is used to accurately estimate its temporal location. The use of the proposed sensor and it interrogation

system for temperature and refractive index sensing is performed. A theoretical model is developed, which is validated by an experiment in Chapter 4.

1.2 Major Contributions of This Thesis

In this thesis, two novel real-time interrogation systems based on WTT mapping with high interrogation speed, resolution and stability are proposed and experimentally demonstrated. The major contributions include:

1) A HBRG sensor is proposed which is used for measuring the temperature and strain simultaneously. The random grating provides a random distribution in its reflection spectrum. Via WTT mapping, a random microwave waveform is generated in which the sensing information is encoded as a temporal waveform shift. By using pulse compression technique, the temporal waveform shift can be monitored with a highly improved resolution, while the SNR of the sensing signal is also improved significantly. A theoretical model is developed, which is validated by an experiment in Chapter 3. Experimental results show that the proposed sensor can provide a stain and temperature resolution better than 7.1 με and 0.79°C at an ultra-high speed of 20 MHz.
2) An LCFBG used in a complementary manner is designed and employed in a HBRG sensor, to provide complementary optical dispersion, to make two WTT mapped temporal pulses experience positive and negative time delays. By measuring the temporal waveform shifts of the two temporal pulses, the stain and temperature information can be retrieved simultaneously. Without using any interferometer structure, the system is ultra-stable. A theoretical model is developed, which is validated by an experiment in Chapter 3.
3) A high Q factor microdisk resonator is designed and used as a silicon photonic refractive index sensor. By adding a slab waveguide surrounding the disk and the bus

waveguide, the interaction between the light field and the sidewalls of the disk is weakened, then the scattering introduced by the sidewall roughness is suppressed and a higher Q factor is archived, leading to an improved detection sensitivity. A theoretical model is developed, which is validated by an experiment in Chapter 4. The measured Q factor of a fabricated microdisk is 172400 (in air) and 40000 (in water). Experimental results show that the sensor has a sensitivity of 76.8 pm/℃ and a resolution of 0.234 ℃ as a temperature sensor, and a sensitivity of 33.28 nm/RIU and a resolution of 1.32×10^{-3} RIU as an refractive index sensor. The interrogation speed is as high as 100 kHz.

4) By using a POF, built using a reference signal, and a Hamming window, the SNR of the obtained filtered waveform can be improved significantly. Thus, the measuring accuracy of the interrogation system can be improved. A theoretical analysis is given, and experimentally approved in Chapter 4.

1.3 Organization of This Thesis

The thesis consists of five chapters. In Chapter 1, a brief introduction to optical sensors including optical fiber sensors and integrated optical sensors is presented, and the recently proposed interrogation techniques are reviewed. The challenges in the current interrogation systems are outlined, and the motivation of the thesis to tackle these challenges is given. The major contributions of this research are then summarized.

In Chapter 2, a technical overview for optical sensors including fiber grating sensors and silicon photonic sensors is presented, and different interrogation techniques are discussed.

In Chapter 3, an approach to interrogate a strain and temperature random grating sensor with high speed and high resolution is proposed. Experimental results show the sensitivities of the random grating sensor are 31.48 ps/°C and 3.5 ps/με, the resolutions better than 7.1 με and 0.79°C at a high speed of 20 MHz is experimentally demonstrated.

In Chapter 4, an approach to interrogate MDR sensors for temperature and refractive index information with high speed and high resolution is proposed, and the algorithm for improving the SNR of the generated signal is investigated based on a numerical simulation and experiment results. The experimental results show that the sensor has a sensitivity of 76.8 pm/℃ and a resolution of 0.234℃ as a temperature sensor, and a sensitivity of 33.28 nm/RIU and a resolution of 1.32×10^{-3} RIU as an refractive index sensor. The interrogation speed is as high as 100 KHz.

Finally, conclusions are drawn in Chapter 5, with some perspectives for the future work.

CHAPTER 2 TECHNICAL OVERVIEW

Among different optical sensors, fiber grating sensors and silicon photonic resonator sensors are two important topics. In this chapter, we present a technical overview of the fiber grating sensors and silicon photonic resonator sensors, and introduce different interrogation techniques proposed for these optical sensors.

2.1 Fiber Grating sensors

An FBG is a fiber device in which the refractive index of the fiber core is modulated periodically along the fiber, which is realized by exposure of the fiber core to an intense optical interference pattern at a wavelength in the ultra-violet (UV) region. Under the phase matching condition, the light with forward propagating mode can be coupled to the backward propagating mode by a FBG, and its wavelength is determined by its grating period. Since this period depends on environmental parameters such as temperature, applied strains or pressures, the wavelength of the reflected light is a function of the environmental parameters. By monitoring the wavelength shifts of the reflected light, the change of environment can be revealed. In 1978, the first in-fiber grating structures were first demonstrated by Dr. Hill at the Communications Research Centre (CRC), Canada [45]. After that, numerous researches on fiber gratings are implemented and FBG sensors become one of mainstream optical sensing technologies.

In this section, different types of FBGs and their applications are introduced, whereas the sensing principles of FBG sensors are elaborated.

2.1.1 Classification of fiber Bragg gratings

After decades of research on the fiber gratings, many kinds of fiber gratings are proposed and implemented nowadays. In this section, we will give introductions for uniform FBG, tilted FBG, chirped FBG, sampled FBG, PS-FBG and random grating.

2.1.1.1 Uniform FBG

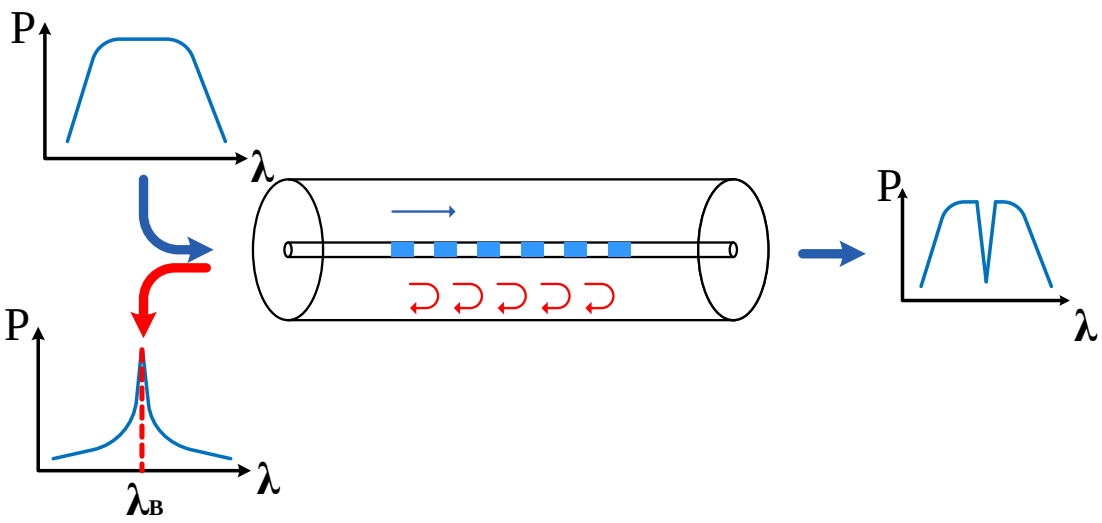

Fig. 2.1 Uniform fiber Bragg grating. The variation of the refractive index of the core is uniform along the axis, and the modulation depth is constant.

An uniform FBG indicates that the periodicity of the grating is uniform along the axis, and the modulation depth of the refractive index is constant, shown in Fig. 2.1. An FBG can couple the light with forward propagating modes to the backward propagating modes at specific wavelength, or its Bragg wavelength. The Bragg wavelength of an FBG depends on the effective index of the fiber core mode and the grating period, and the wavelength bandwidth depends on several parameters, such as the modulation depth and the grating length.

Apart from serving as sensing elements, FBGs are widely used as optical notch filters in optical add-drop multiplexers (OADMs) [46], and used as reflectors and output couplers in fiber lasers [47], [48].

Detailed sensing principles of FBG sensors are discussed in the next subsection.

2.1.1.2 Tilted Fiber Bragg Gratings

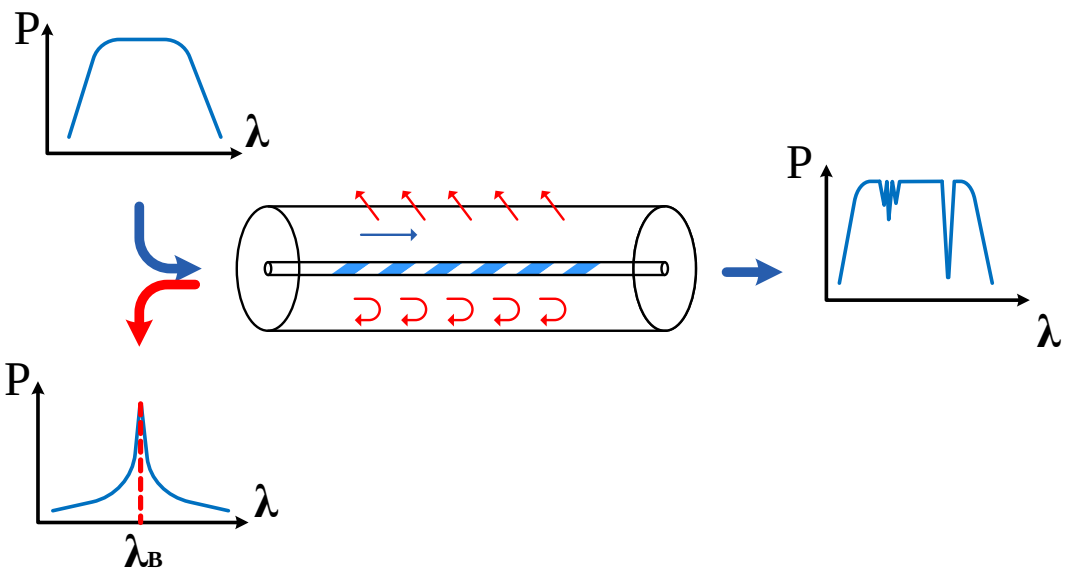

Fig. 2.2 Tilted fiber Bragg gratings. The variation of the refractive index of the core is uniform but has an angle to the axis of the fiber core, and the modulation depth is constant.

Tilted FBGs have similar modulation distributions with the uniform FBGs. However, the variation direction of a tilted FBG has an angle to the axis of the fiber core, as shown in Fig. 2.2. With a part of light reflected in to the fiber cladding, a tilted FBG can couple the forward propagation core modes to backward propagation core modes and backpropagation cladding modes. The propagation losses for the cladding modes are very high, so these lights are noticeable in the transmission spectrum, but not in the reflection spectrum.

Tilted FBGs can be used as photonic fractional temporal differentiators [49], in-fiber polarizers [50], side-tap modal channel monitor in mode division multiplexed systems [51], and various kinds of sensor for temperature [52], strain [53], bending [54], refractive index [55], vibration [56], and so on.

2.1.1.3 Chirped Fiber Bragg Gratings

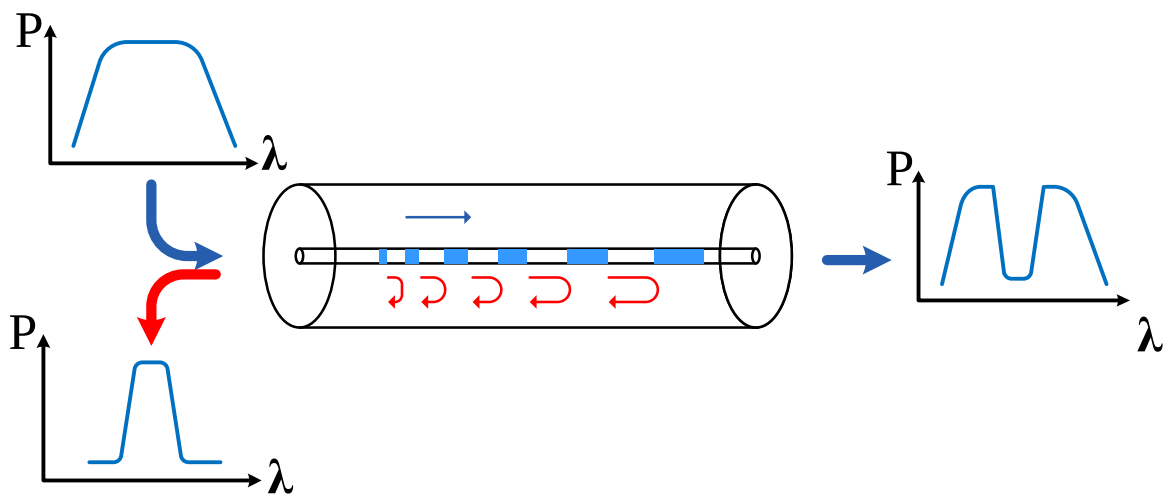

Fig. 2.3 Chirped fiber Bragg gratings. The refractive index of the core has a linear increasing or decreasing variation of the grating period.

As shown in Fig. 2.3, chirped FBGs are realized by varying the grating period linearly, or changing the average refractive index linearly along the length of the fibers [57]. Because of the varying grating periods, a chirped FBG can reflect lights with different wavelengths at different positions, which results in linearly time delays for different reflected wavelengths.

Chirped FBGs are firstly designed for dispersion compensation in optical communication systems [58]. After several years of research, chirped FBGs can find applications in optical pulse generation [59] and processing [60], microwave waveform generation [61] and processing [62], and fiber laser systems [63]. In optical sensing systems, a chirped FBG can serve as a sensing element for measuring the strain and temperature simultaneously by carefully monitoring its reflection spectrum shift and broadening simultaneously. Chirped FBGs can also act as dispersion elements for the WTT mapping in the interrogation system for the optical sensors [64].

2.1.1.5 Phase-Shifted Fiber Bragg Grating

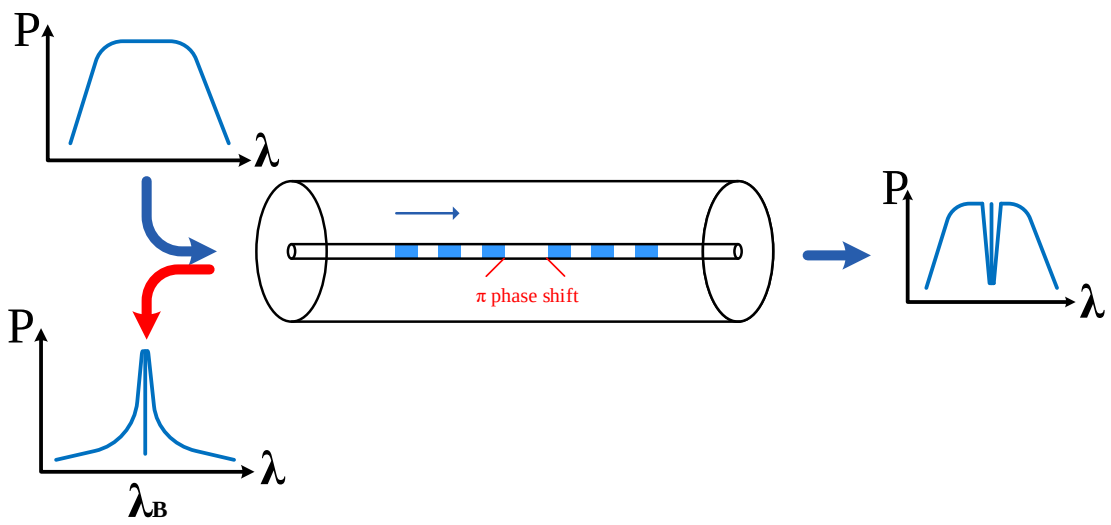

Fig. 2.4 Phase-shifted fiber Bragg gratings. Phase shifts are introduced to refractive index modulation

A PS-FBG is realized by introducing one or multiple phase shifts across the fiber grating, which break the phase matching states between the reflected light from the sub-gratings before and after the shift points. Thus, the sub-gratings form optical cavities, which some specific wavelengths with ultra-narrow bandwidth can go though. By adjusting the locations and magnitudes of the phase shifts, a PS-FBG with a specific transmission spectrum can be realized [65].

PS-FBGs are firstly used as optical filters for wavelength demultiplexing for multichannel light wave systems [65], and then widely used to implement optical temporal differentiators [66], optical temporal integrators [67], Hilbert transformers [68], optical switches [69], and optoelectronic oscillators [70]. The ultra-narrow notch in the reflection spectrum also gives the

PS-FBG sensor an ultra-high sensing resolution. Thus, the PS-FBGs are used to the detection of vibration [71], ultrasound [72], and liquid refractive index [73].

2.1.1.6 Sampled Fiber Bragg Gratings

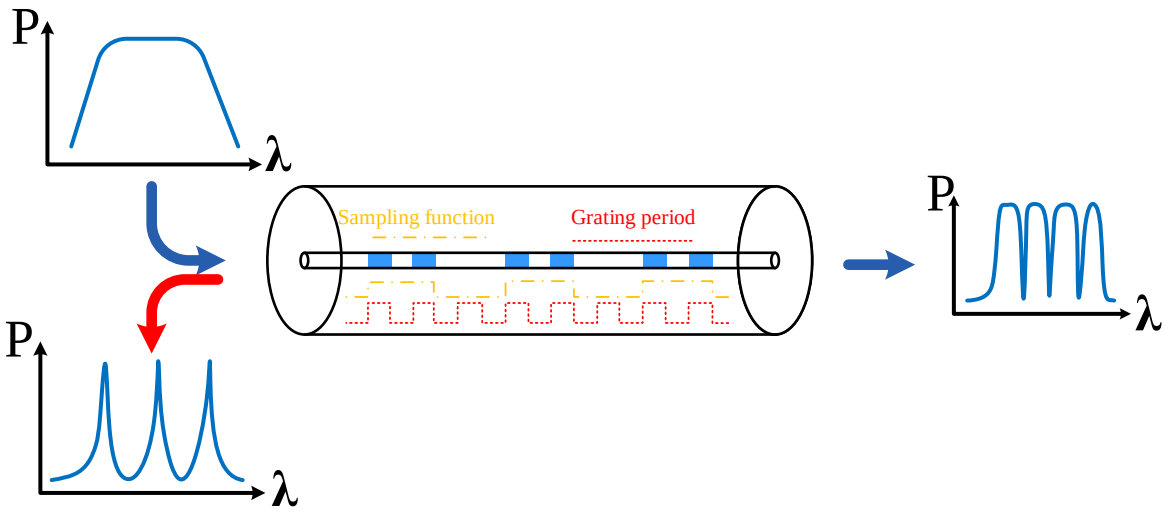

Fig. 2.5 Chirped fiber Bragg gratings. The variation of the refractive index of the core is modulated by a sampling function.

A sampled FBG is realized based on a conventional grating at the appropriate wavelength multiplied by a sampling function, as shown in Fig. 2.5. Multiple frequency wavelengths can be reflected when a uniform sampling function is applied, with a free spectrum range (FSR) determined by the period of the sampling function [74]. Changing the profile of the sampling functions, equivalent chirped FBGs [75] and equivalent phase-shifted FBGs [76] can be realized, with a released requirement for the fabrication.

Sampled FBGs are firstly reported and used in an integrated distributed Bragg reflector (DBR) laser by Larry Coldren [74], and then be used as multichannel filters in DFB lasers [77]

and wavelength division multiplexing (WDM) systems [78]. Because the transverse load on the fiber only has an influence on the grating but not on the sampling function, sampled FBGs can be used as a transverse load sensor which is independent to the environment noises such as temperature, strain and vibration [79].

2.1.1.6 Fiber Random Gratings

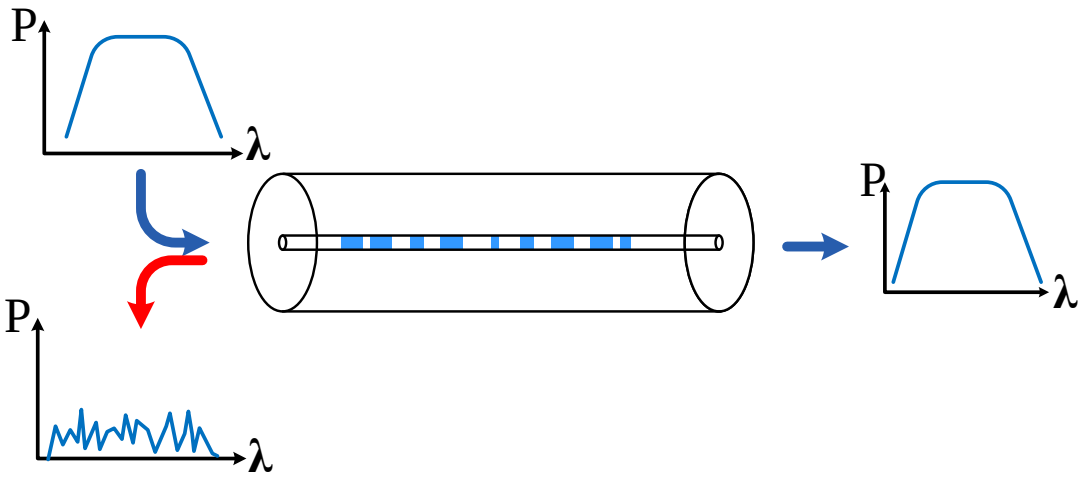

Fig. 2.6 Fiber random gratings. The refractive index of the core is modulated by a pseudo-random sequence.

A random grating is fabricated by pseudo-randomly varying the grating period of a FBG. As shown in Fig 2.6, the reflection spectrum shows a totally random distribution, but the intensity is very small, leading to an almost flat top transmission spectrum. When the temperature and the applied strain is changed, the reflection spectrum of the random grating will shift. Cross-correlation can be used to interrogate the spectrum shifts of the random grating [19], but the interrogation resolution is still limited by the used OSA and the interrogation speed is very low for sweeping such a large wavelength range (~100 nm).

For different applications, there are many other kinds of FBGs, such as writing gratings in multimode fibers [80], birefringent fibers [81] and so on. In Section 2.1.2, the basic principle of the FBG is introduced, so that the principles of other different kinds of FBG could be understood.

2.1.2 Sensing Principles of Fiber Bragg Grating

The basic operation principle of an FBG sensor system is to monitor the wavelength shift of the reflected signal where the sensing information is encoded. The resonant wavelength, or the Bragg wavelength λ_B of an FBG, is given as [82]:

$$\lambda_B = 2n_{eff}\Lambda \tag{2-1}$$

where n_{eff} is the effective refractive index of the fiber core mode, and Λ is the grating period. When a broadband lightwave is fed into such an FBG device, a narrowband spectrum component at the Bragg wavelength is reflected by the FBG, resulting in a peak in the reflection spectrum and a notch in the transmission spectrum. From (2-1), it can be seen that the Bragg wavelength is determined by the effective refractive index and the length of grating period, which are sensitive to the environment. The perturbation of the FBG leads to a shift in the Bragg wavelength, which can be detected in the transmission spectrum and the reflection spectrum.

Most of the work on FBG sensors are used for sensing of strain and temperature. The strain response arises because of both the physical elongation of the grating (corresponding to the change in grating period) and the change in effective refractive index due to photoelastic effects, whereas the temperature response arises for the inherent thermal expansion of the fiber and the temperature

dependence of the refractive index. Thus, the shift in Bragg wavelength with strain and temperature can be expressed with [21]:

$$\Delta\lambda_B = 2n_{eff}\left(\left\{1-\frac{n_{eff}^2}{2}\left[P_{12}-\nu\left(P_{11}+P_{12}\right)\right]\right\}\varepsilon+\left[\alpha+\frac{\left(\frac{dn_{eff}}{dT}\right)}{n_{eff}}\right]\Delta T\right) \tag{2-2}$$

Where ε is the applied strain, $P_{i,j}$ coefficients are the Pockel's coefficients of the stress-optic tensor, ν is Poisson's ratio, α is the coefficient of thermal expansion (CTE) of the fiber material, and ΔT is the temperature change. For a normal silica fiber, the measured strain response at a constant temperature is found to be [21]:

$$\frac{1}{\lambda_B}\frac{\delta\lambda_B}{\delta\varepsilon} = 0.78\times10^{-6}\,\mu\varepsilon^{-1} \tag{2-3}$$

and the thermal response at a constant stain is found to be [21]:

$$\frac{1}{\lambda_B}\frac{\delta\lambda_B}{\delta T} = 6.67\times10^{-6}\ ^{\circ}\mathrm{C}^{-1} \tag{2-4}$$

Thus, the typical strain response of an FBG near the wavelength of 1550 nm is ~ 1.2 pm/με, and the typical temperature response of an FBG near the wavelength of 1550 nm is ~ 13 pm/°C [83].

2.2 Silicon Photonic Resonators

Silicon photonic resonators are implemented by fabricating optical cavities on silicon-on-insulator substrates. Different types of silicon photonic resonators have been proposed and demonstrated. A WBG is a fundamental component, which is usually implemented by varying the dimensions of the waveguide periodically to realize a periodic refractive index modulation as the same as in the FBG [84]. A ring/racetrack resonator is another commonly studied resonator, which couples the fed light wave from the bus waveguide to a ring via evanescent field coupling. When a broadband light is introduced to an MRR, the wavelength components under the phase matching condition can be totally coupled and held in the ring, leading to notches in the transmission spectrum [85]. Since the length and the effective refractive index of waveguides depend on environmental parameters such as temperature and cladding refractive index, the wavelength of the transmitted light is a function of the environmental parameters. Monitoring the wavelength shifts of the transmitted light, the change of environment can be revealed. Basing on the waveguides with dimensions smaller than the free-space wavelength of light, the evanescent field at the waveguide surface extends a few hundred nanometers into the surrounding [86][87]. The interactions with molecules in proximity or surface will change the effective refractive index of the propagation mode, and the interaction length can be multiplied by the number of roundtrips by the light in the resonator [87]. Therefore, with an enhanced refractive index sensitivity, silicon photonic resonators have great potential as biosensors for medical, point-of-care and home healthcare diagnostic applications.

In this section, different type of silicon photonic resonators and their applications are introduced, whereas the sensing principles of resonator sensors are elaborated.

2.2.1 Classification of Silicon Photonics Resonators

After several years of research on the silicon photonics, numerous resonators have been proposed and implemented. In this section, we will give introductions to ring resonators, slot waveguide ring resonators, Bragg grating resonators and microdisk resonators.

2.2.1.1 Micro-ring Resonators

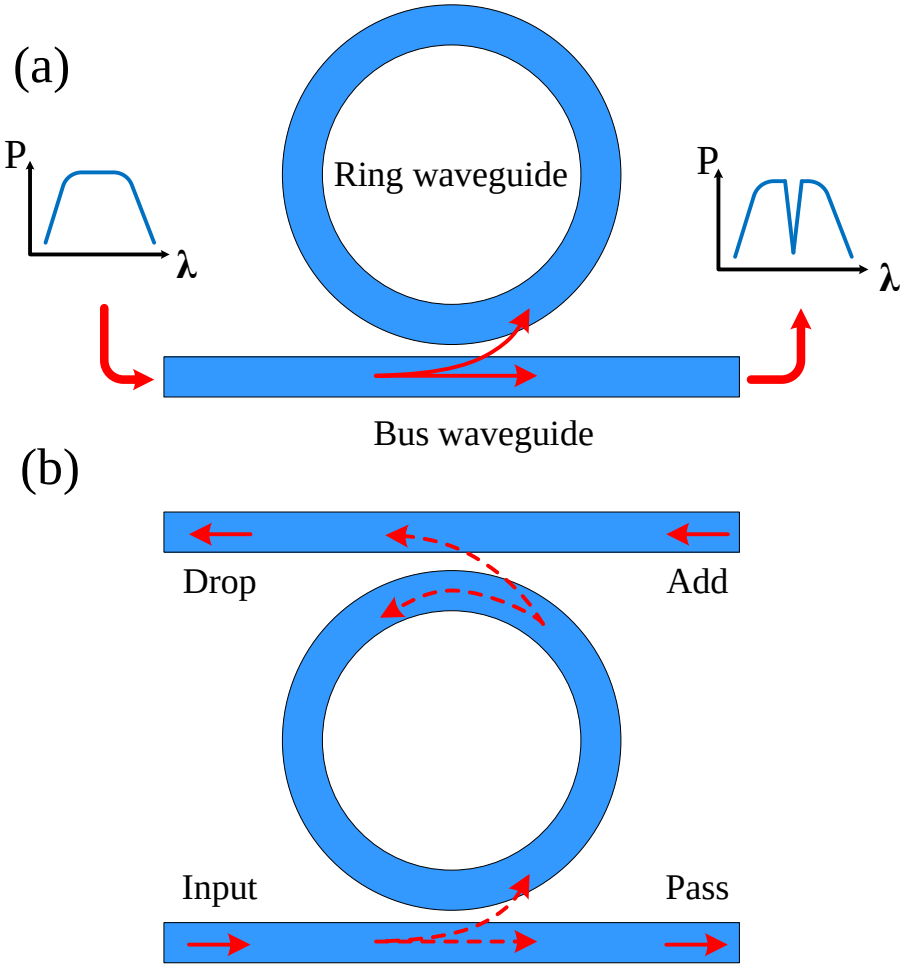

Fig. 2.7 (a)All-pass micro-ring resonator; (b) add-drop ring resonator.

A simplest form of an MRR is called all-pass MRR, which is constructed by a looped optical waveguide, known as a ring, and a bus waveguide to access the loop, as shown in Fig 2.7 (a). Via evanescent field coupling, the incident light wave propagating along the bus waveguide would be coupled into the ring waveguide. If the light wave in the ring experience a round trip phase shift that equals an integer times of 2π, the light waves in the ring and in the bus waveguide interfere with each other, leading to notches in the transmission spectrum. If the light wave does not match the phase condition, it would be transmitted through the bus waveguide. The resonant wavelengths are determined by the length of the ring and the refractive index of the guided modes.

Another typical MRR is add-drop MRR, where the ring resonator is coupled to two waveguides, which is shown in Fig. 2.7 (b). Thus, the light wave at the resonant wavelength can be coupled partially at the drop port, which can be utilized in a WDM system [88]. In order to meet different requirements, devices with multiple coupled or cascaded MRRs have been proposed and implemented. Via tuning the configurations of the individual rings and the coupling coefficients between the rings with the bus waveguides, devices with tailored spectrums can be realized for specific applications, such as flat-top filters [89], multi-bit delay lines [90] or high sensitivity sensors [91].

In sensing applications, the MRR is widely used for the detection of temperature [92] and refractive index [31] for its high sensitivity. With special designed mechanical systems, strain [93][95], and vibration [94] can also be measured by using MRRs.

2.2.1.2 Slot Waveguide Microring Resonators

A slot waveguide MRR is implemented by forming an MRR with slot waveguides instead of strip waveguides, as shown in 2.8 (a). The mode profile is shown in 2.8 (b), from which it can be noted that the light wave is mainly confined in the cladding between the two waveguides. Therefore, any interaction with molecules in the cladding will change the effective refractive index of the guided mode significantly, leading to an extremely high sensitivity for refractive index sensing. However, the interactions in the cladding cause strong scatterings, leading to a high propagation loss.

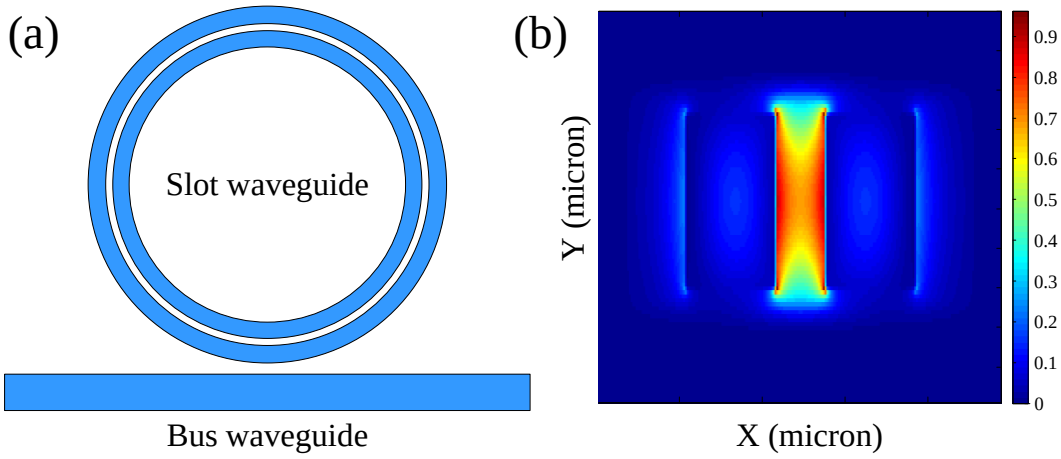

Fig. 2.8 (a)All pass slot waveguide micro-ring resonator; (b) mode profile in slot waveguide.

Various kinds of biosensors have been proposed using slot-waveguide microring resonators with enhanced sensitivity [95] [96]. But the high propagation loss leads to a low Q factor, which results in a low detection resolution.

2.2.1.3 Waveguide Bragg Gratings

Grating structures are also accessible in silicon photonics. Fig 2.9 shows the structure of the simplest type of integrated Bragg grating: a uniform strip WBG. In the uniform strip WBG, the grating and the waveguide are defined in a single layer, and the refractive index modulation is realized by varying the width of the waveguide [97]. The modulation depth is determined by the width of corrugations (ΔW), and the grating period is determined by the period of the corrugations (Λ). As a uniform FBG, the uniform WBG can couple the forward propagating mode to backward propagation mode at its Bragg wavelength. Other kinds of FBGs can also be implemented in silicon photonics. For example, a chirped WBG can be realized by changing the width or period of corrugations linearly, and a phase shifted WBG can be designed by adding phase shifts in the period of corrugations.

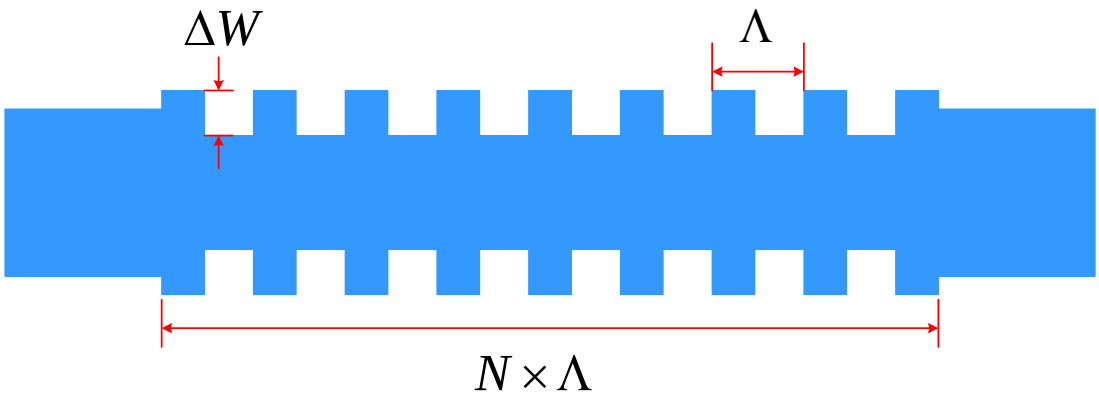

Fig. 2.9 Uniform strip waveguide Bragg grating.

WBGs are firstly demonstrated in 2001 by Murphy [84] and soon find applications in optical modulation [98], and microwave generation [99]. In the meantime, the WBGs are also used for the temperature sensing [100], chemical sensing [29] and biosensing [30].

2.2.1.4 Micro-disk resonator

An MDR is realized by replacing the ring waveguide in the MRR by a small disk, which is still a looped waveguide, as shown in Fig. 2.10 (a). The mode profile of the fundamental guided mode is shown in Fig. 2.10 (b). As can be seen, only one sidewall exists along the propagating paths. Therefore, the scattering introduced by the sidewall roughness is reduced, resulting in a lower propagating loss [101]. The radius of the disk is commonly set as ~ 3 μm to reduce the number of modes, which results from lacking one boundary.

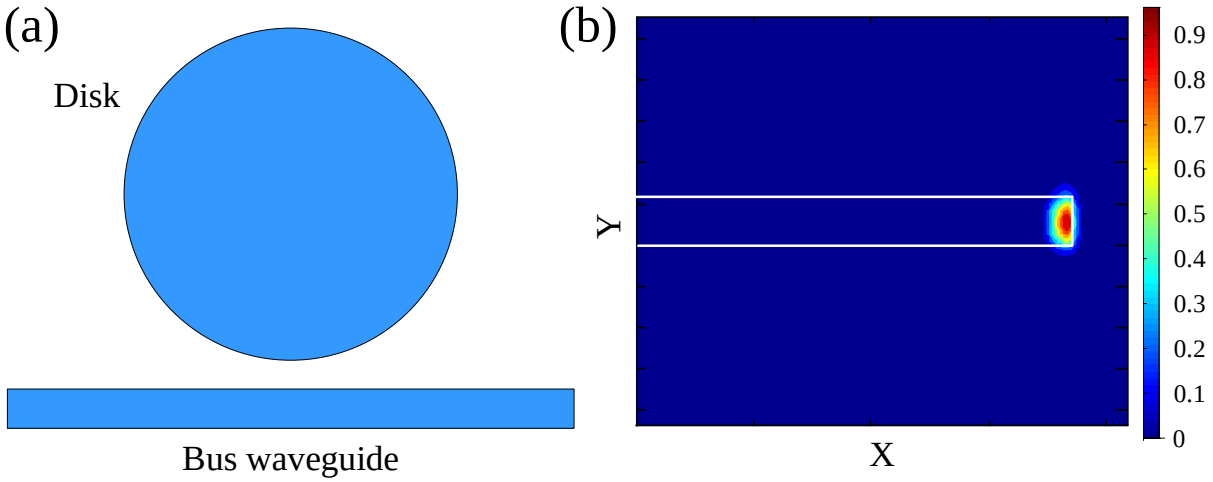

Fig. 2.10 (a) Micro-disk resonator; (b) mode profile in microdisk.

The first MDR was firstly proposed in 2005 [101]. Because of the ultra-compact size and the ultra-low power consumption, the MDRs are ideal for acting as modulators and switches [102].

Meanwhile, the MDR with an ultra-high Q factor can offer a low detection resolution acting as an optical sensor [32].

Although different types of silicon photonic resonators are proposed and demonstrated for various sensing applications, the basic principles are based on evanescent field sensing of silicon waveguides. In Section 2.2.2, the sensing principles of MRRs are introduced, so that the principles of other different kinds of MRR, slot waveguide MRR and MDR can be understood, and the principle of WBGs is similar to that of FBGs, which is introduced in Section 2.1.2.

2.2.2 Sensing Principles of Microring Resonators

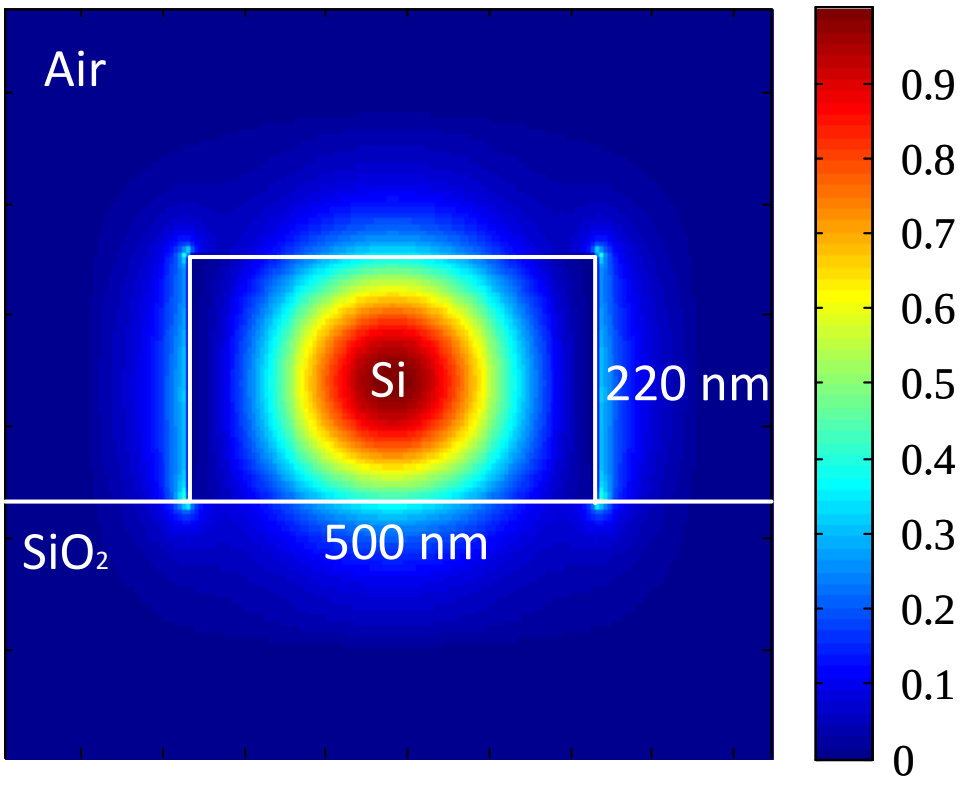

Fig. 2.11 Fundamental mode profile in a strip silicon waveguide at 1550 nm.

The resonant wavelength of a MRR can be calculated as:

$$\lambda_{res} = \frac{2\pi R}{m} n_{eff} \tag{2-5}$$

where λ_{res} is the resonate wavelength, R is the ring radius, m is the integer mode order and n_{eff} is the effective index of the guided mode of the ring waveguide. From (2-5), it can be seen that the resonant wavelengths are determined by the length of ring and the effective refractive index of the waveguide.

The refractive index sensing is based on evanescent field sensing of silicon waveguides. When light propagates into an optical waveguide, a large amount of optical power is coupled into the core, while the remainder is confined into the cladding and substrate regions, as shown in Fig. 2.11. The effective refractive index of the propagating mode also depends on the concentration of the specific analyte localized near the sensor surface, because of the interaction between the evanescent tail of a guided mode and the analyte [86]. Thus, the magnitude of the effective refractive index change is related to the percentage of field interacting with the analyte [103]. For a slot waveguide, majority optical power is confined in the cladding between the two waveguides, leading to an enhanced sensitivity, as shown in Fig. 2.8 (b). For an MRR, the degree of interaction of the evanescent field and the analyte is the product of the length of the ring and the number of roundtrips by the light inside the ring. Thus, a high Q MRR comes to be a high sensitivity sensor.

The change of the refractive index of the cladding (Δn_{clad}) is encoded in the shift of the resonant wavelength of the resonator, which is given by

$$\Delta\lambda_{RI} = \frac{\lambda_{res}}{n_g} \Delta n_{clad} \frac{\partial n_{eff}}{\partial n_{clad}} \tag{2-6}$$

where n_g is the group index of the guided mode of the waveguide, n_{clad} is the refractive index of the cladding.

The temperature variation also has an influence on the resonant wavelengths of an MRR. When temperature changes, the effective refractive index of the guided mode changes with the temperature due to the thermo-optic effect, and the radius of the ring waveguide also changes because of the thermal expansion effect. Therefore, the overall wavelength shift introduced by the temperature change is expressed as [104]:

$$\Delta\lambda_{Temp} = \frac{\lambda_{res}}{n_g} \Delta T \left(\alpha_{si} n_{eff} + \frac{\partial n_{eff}}{\partial T} \right) \tag{2-7}$$

where ΔT is the temperature change, α_{si} is the thermal expansion coefficient and $\partial n_{eff} / \partial T$ is the thermo-optic coefficient.

For an MDR sensor, the principle is almost the same as that of the MRR sensor.

2.3 Interrogation techniques

As stated in section 2.1 and 2.2, the sensing information is encoded in the wavelength shifts of the FBG sensors and silicon photonic resonator sensors. Therefore, a spectrum analysis is required to demodulate or interrogate the sensing signal. An OSA is the most straightforward device for the spectrum measurement, but the offered resolution is very limited. Meanwhile, the wavelength scanning speed of an OSA is too slow to interrogate the fast-changing sensing signal. Therefore, indirect measurements for the spectrum are needed for the high-speed and high-resolution interrogation of optical sensors.

To date, many interrogation systems for FBG sensors are proposed and experimentally demonstrated, and most of them can be used for the interrogation of silicon photonic sensors. These interrogation systems are based on converting the optical wavelength shifts to the changes of other parameters in optical domain or in electrical domain. In this section, several interrogation systems are reviewed.

2.3.1 Interrogation in Optical Intensity Domain

By utilizing optical edge filters, tunable filters or scanning devices incorporating with optical interference structures, the optical wavelength shift can be converted to the optical intensity change, which can be easily monitored with a high-speed PD.

2.3.1.1 Optical edge filter

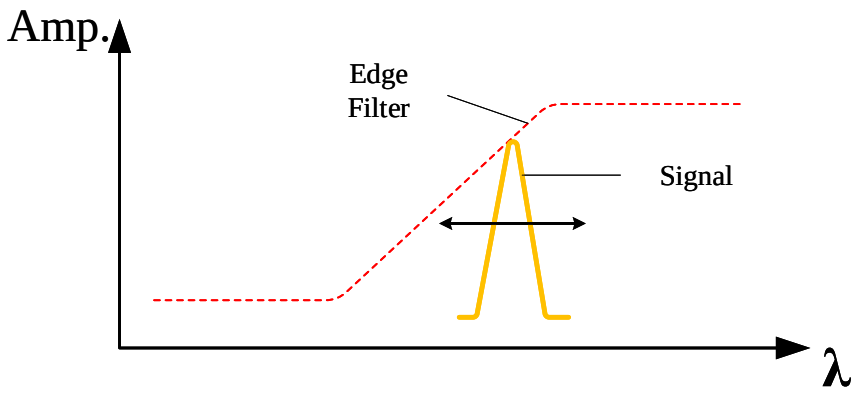

Fig. 2.12 Principle of the edge filter method.

The simplest way to translate the optical wavelength shifts to optical intensity changes is to use a linearly wavelength-dependent optical edge filter, whose transmission spectrum is shown in Fig. 2.12 [35] [36] [105] [106]. As can be seen, the intensity of the output light is a function of the wavelength. By measuring the intensity changes of the output, the wavelength shifts are revealed. This kind of systems is simple and stable, but the detection resolution is inversely proportional to the measuring range.

Fig 2.13 shows an interrogation system for a FBG sensor based on an edge filter. A broadband light is fed to a FBG sensor, and the reflected light is split into two beams, with equal intensity. The 50:50 coupler are wavelength-independent on the required wavelength range, which indicates the splitting ratio is constant. One beam is fed to a PD directly, as a reference, whereas the other beam is filtered by the linear edge filter before the detection, as a signal. The transfer function of the edge filter is linear over a wavelength range, which decides the measuring range of the sensing system, and the slope of the filter determines the interrogation resolution. The ratio of

the intensities of the signal beam and the reference beam indicates the wavelength of the reflected light, meanwhile the noises introduced by power variation of the light source, the uncertain insertion loss of the connectors and other fluctuations can be eliminated. The ratio between the signal intensity, I_S , and the reference intensity, I_R , can be expressed as [105]

$$\frac{I_S}{I_R} = A\left(\lambda_B - \lambda_0 + \frac{\Delta\lambda}{\sqrt{\pi}}\right) \tag{2-8}$$

where A is the slope of the edge filter, λ_0 is the starting wavelength of the edge filter, λ_B is the Bragg wavelength of the FBG and $\Delta\lambda$ is the linewidth of the FBG. This system is simple and stable, and a resolution of 375 με has been demonstrated with a measurement range of 11 mε [105].

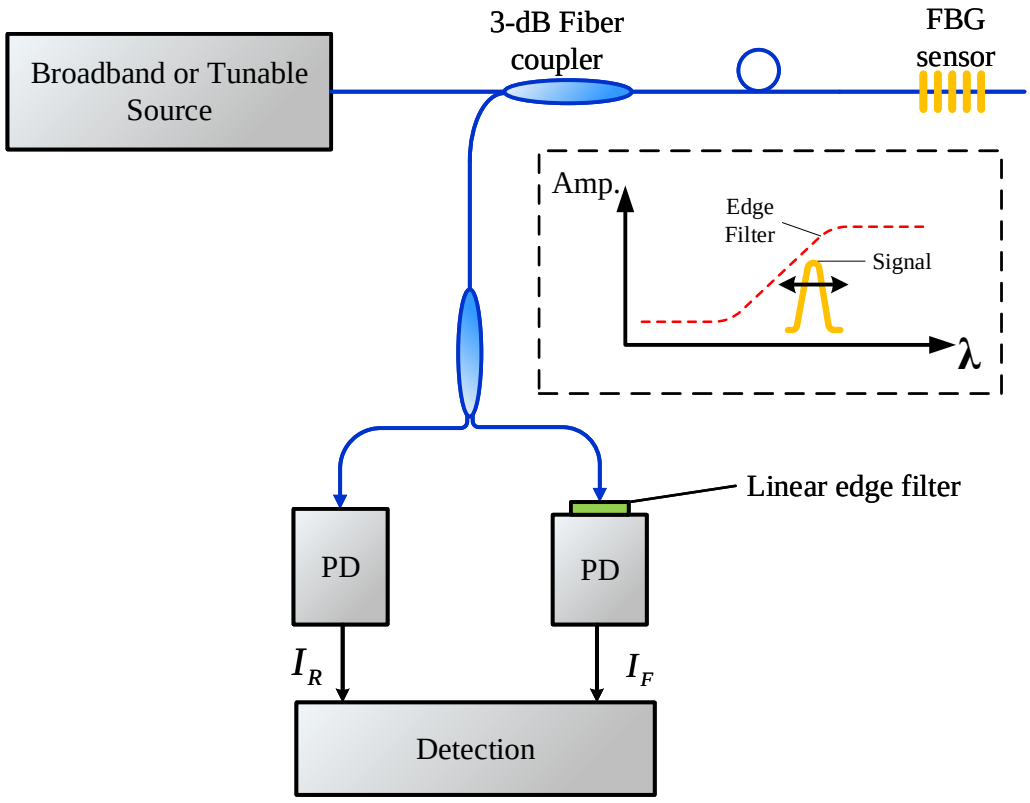

Fig. 2.13 Block diagram of an interrogation system based on a linear edge filter [105].

2.3.1.2 Tunable optical filter

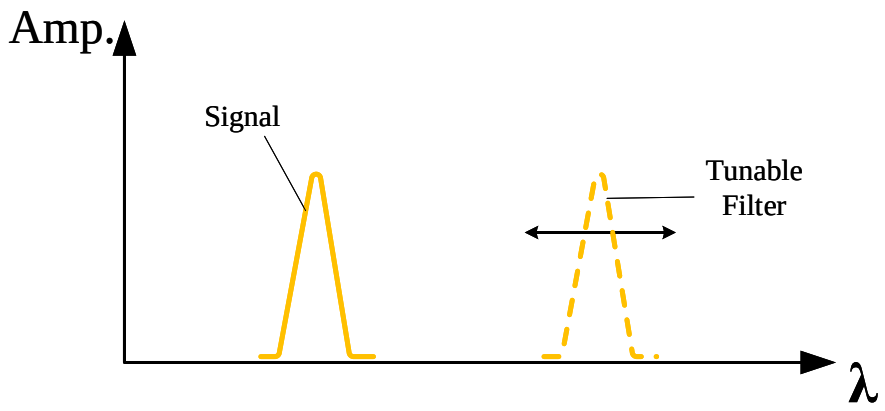

Fig. 2.14 Principle of the tunable optical filter method

A tunable filter can be used to detect the wavelength of a FBG sensor. The basic principle is shown in Fig. 2.14. When the spectrum of the tunable filter matches that of the FBG, the intensity of the output reaches a peak value. By measuring the location of the peak and the corresponding wavelength shift of the tunable optical filter, the wavelength shift of the FBG sensor is revealed [17]. The interrogation resolution is determined by the SNR of the light reflected by the FBG sensor, and the linewidth of the tunable optical filter. The measuring range depends on the FSR of the tunable optical filter.

Fig. 2.15 shows an interrogation system for a FBG sensor based on a tunable Fabry-Perot filter. A broadband light is fed to a FBG sensor, and the reflected light is directed to a tunable Fabry-Perot cavity. By using a piezoelectric element to tune the length of the cavity, the passband of the Fabry-Perot filter can be locked to the spectrum of the FBG sensor. Then, the corresponding control voltage of the tunable Fabry-Perot filter indicates the wavelength of the FBG sensor. This system provides a resolution of ~1 pm over a detection range of 43 nm [17].

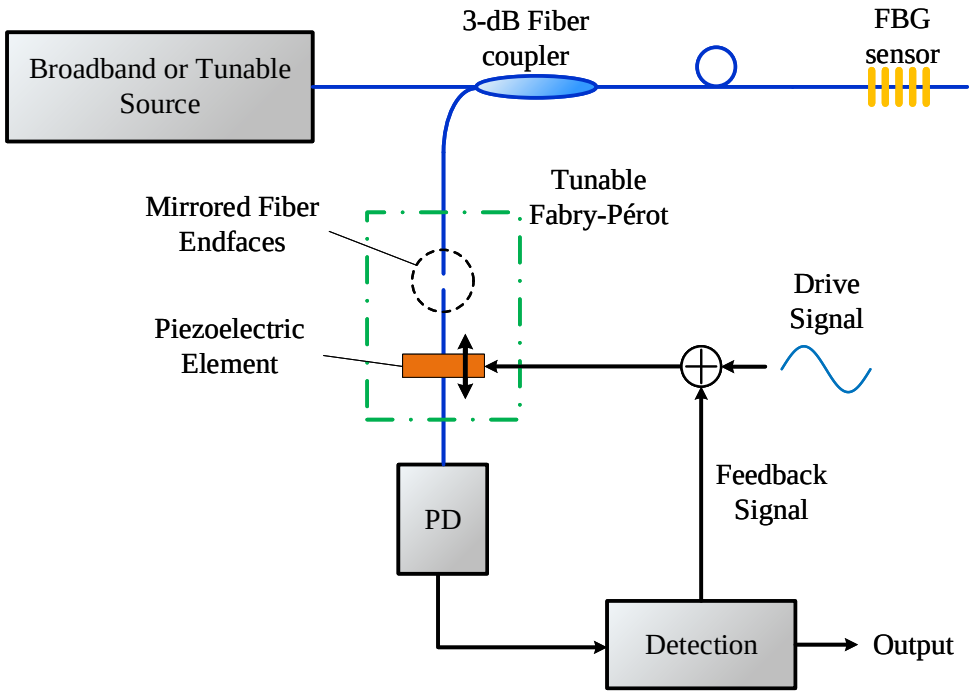

Fig. 2.15 Schematic diagram of an FBG interrogator based on a tunable Fabry-Pérot filter [17].

2.3.1.3 Unbalanced interferometer

An unbalanced optical interferometer can be used to convert the wavelength shift of the FBG sensor to the phase shift of the interference signal, which can be easily measured by a DSO or a phase meter with a significantly improved resolution [107] [108] [109]. The interference signal of an unbalanced optical interferometer, which is shown in Fig. 2.16, is given as [107]:

$$I = B\left\{1 + k\cos\left[\varphi(\lambda) + \phi\right]\right\} \tag{2-9}$$

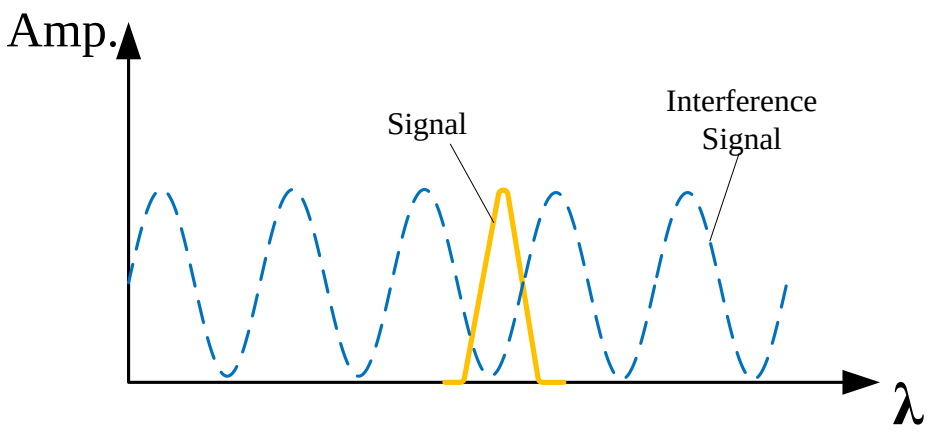

Fig. 2.16 Principle of an FBG interrogator based on unbalanced interferometers.

where $\varphi(\lambda)=2\pi n_{eff}\Delta L/\lambda_B$, B is proportional to the intensity and system losses, ΔL is the length imbalance between the arms, λ_B is the wavelength of the reflected light and ϕ is a bias phase offset of the unbalanced interferometer. From (2-9), it could be see that the wavelength shift of the FBG sensor would introduce a change in optical phase of the interference signal, which is expressed as [107]:

$$\Delta\varphi(\lambda)=-\frac{2\pi n\Delta L}{\lambda_B^2}\Delta\lambda_B \tag{2-10}$$

Thus, driving the interferometer with 2 π phase shift by a piezoelectric element on one arm, the optical phase shift of the interference signal $\Delta\varphi(\lambda)$ can be measured, and then the wavelength shift of the FBG sensor can be obtained.

Fig. 2.17 shows an interrogation system for a FBG sensor based on an unbalanced Mach-Zehnder interferometer. A broadband light is fed to a FBG sensor, and the reflected light is directed to an unbalanced Mach-Zehnder interferometer. By using a piezoelectric element to

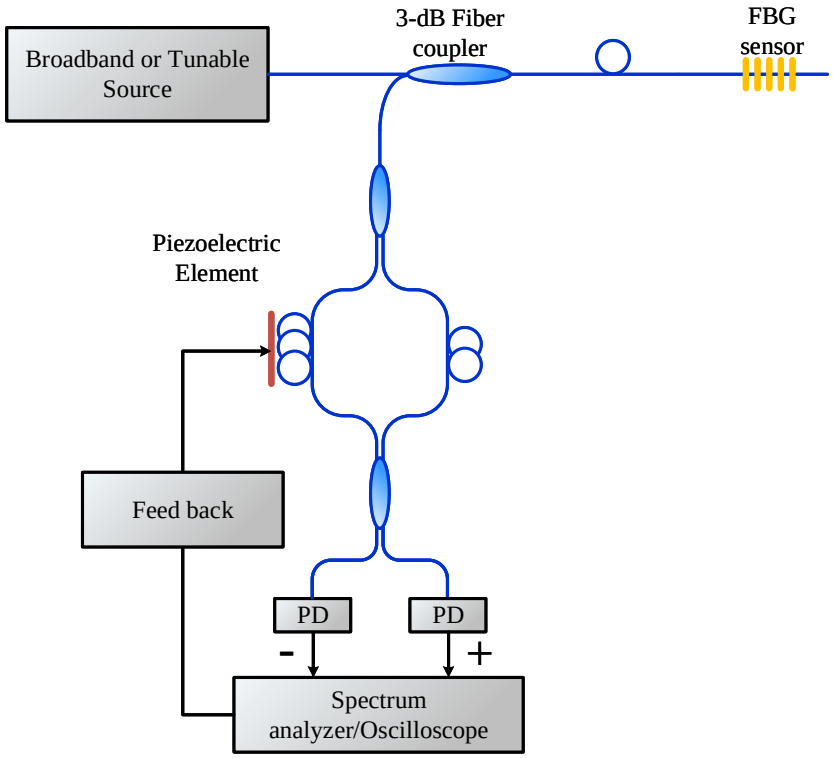

Fig. 2.17 Schematic diagram of an FBG interrogator based on an unbalanced interferometer [107].

a 2π phase shift to the interferometer, the output signal can be measured by a DSO, and its phase shifts indicate the wavelength shift of the FBG sensor. The system provides a strain resolution of ~ 0.6 nεHz$^{-1/2}$ at a frequency of 100 Hz.

Although the systems described above show an improved interrogation resolution, the interrogation accuracy is limited by the noises introduced by the system, especially when the SNR is low.

2.3.2 Interrogation in Electrical Frequency Domain

Utilizing a MPF structure or optoelectronic resonance can convert the wavelength shift of the optical sensors to the frequency shift of an electrical signal in the electrical frequency domain, which can be interrogated by a spectrum analyzer with an ultra-high resolution.

2.3.2.1 Microwave photonic filter

An optical filter with a notch in the spectrum could be used to realize a microwave photonic bandpass filter, and the central frequency of the bandpass filter is a function of the central wavelength of the notch filter [110], [111]. As shown in Fig 2.18 (a), a light wave with a central frequency of f_0 from the TLS is sent to a PM. The PM is driven by a sinusoidal microwave signal with a tunable frequency by a vector network analyzer (VNA). Then, the modulated light wave is introduced to an optical notch filter, with a central wavelength of f_{notch}. By filtering out one sideband of the modulated signal (say, the lower sideband), phase modulation to intensity modulation (PM-IM) conversion is implemented. By feeding the signal to a PD, a microwave bandpass filter is realized, with a central wavelength which can be expressed as:

$$f_{\varepsilon} = f_0 - f_{notch} \tag{2-11}$$

From (2-11) we can see that, the wavelength shift of the notch filter, which can be a FBG, a PSFBG or a MRR sensor, can be converted to the passband frequency change of the MPF. A VNA could be used to monitor the frequency response of the microwave photonic filter, with a resolution of 1 Hz (Keysight E8364A), which corresponding to a resolution of 8×10^{-12} nm at the

wavelength of 1550 nm. The interrogation range is limited by the bandwidth of the VNA, which is 50 GHz, corresponding to 0.04 nm at the wavelength of 1550 nm.

Although an extremely high interrogation resolution is provided by this system, the interrogation speed is limited by the scanning speed of the VNA, and the cost is also very high.

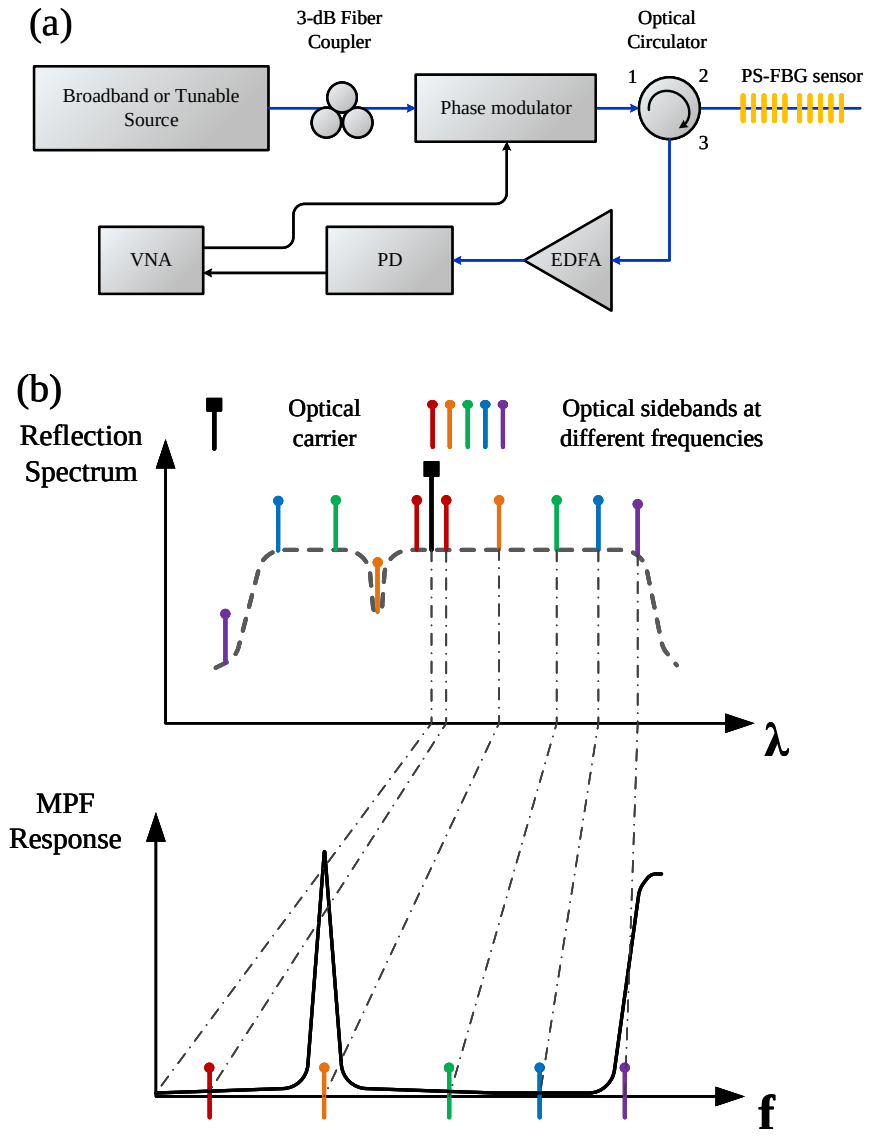

Fig. 2.18 (a) Schematic of a MPF based on phase modulation and optical notch filter; (b) illustration of the operation of the MPF.

2.3.2.2 Optoelectronic oscillator

Using a MPF combining with electronic amplifiers could realize an optoelectronic oscillator to interrogate the optical sensor, which can generate a microwave signal with a frequency determined by the passband of the MPF. Using a microwave spectrum analyzer to monitor the generated signal, the central frequency of the MPF is obtained, and the central wavelength of the optical sensor is revealed, with a significantly increased interrogation speed [112].

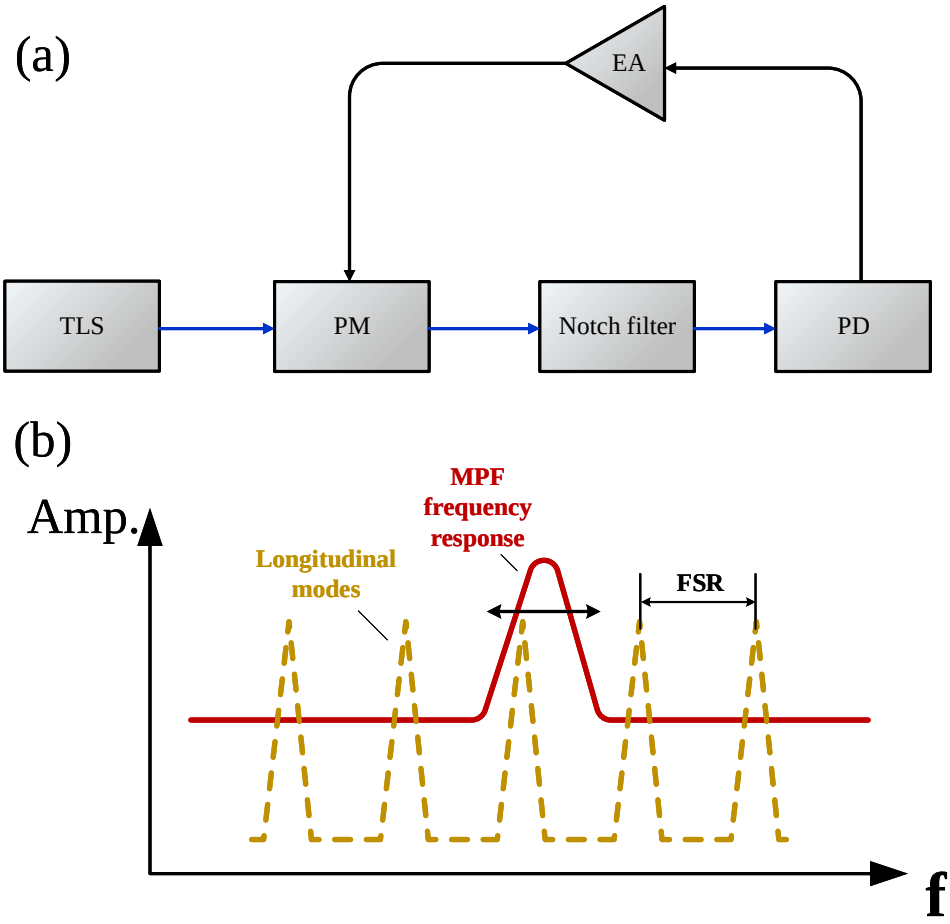

Fig. 2.19 (a) Schematic of an OEO; (b) principle of an OEO. Dash line indicates the longitudinal modes of a ring resonator. Red line is the frequency response of a MPF.

Fig. 2.19 (a) shows a basic structure of an OEO based on phase modulation and optical notch filter. The optical path, consisting of a TLS, a PM, a notch filter and a PD, works as a tunable MPF. By feeding back the output microwave signal generated by the PD to the PM as the modulation signal, an optoelectronic resonance loop is constructed. The electronic amplifier (EA) is used to compensate the electrical loss in the resonance loop. Similar to ring architectures, this resonance loop can also perform a mode selection, which is shown in Fig 2.19 (b). The frequency response of the MPF in corporation with the gain profile of the total system is used to further select the resonance modes. By carefully control the loop gain, only one longitudinal mode can exist in the resonant loop. When the central frequency of the MPF changes, the frequency of the existing mode also changes, which can be monitored by a microwave spectrum analyzer in a short time.

The resolution of the OEO interrogation system is determined by the FSR of the longitudinal modes, which is given as

$$FSR = \frac{2\pi c}{l_{eff}} \tag{2-12}$$

where c is the velocity of light in vacuum, l_{eff} is the effective length the resonator. Typically, the physical length of an OEO, including the optical and electrical paths, can be several kilometres, corresponding to an FSR about 100s KHz (10^{-6} nm). The interrogation range is limited by the working range of the MPF and the EA, which can reach up to 50 GHz in these days. The interrogation speed depends on the scanning speed of the spectrum analyzer.

Fig. 2.20 shows a schematic diagram of an OEO for strain sensing [113]. A light from a laser source is fed to a PM. A two-port PM is used, which makes the MPF as a two-tap microwave

filter with a reduced bandwidth. The phase-modulated light is sent to a PS-FBG via an optical circulator (OC) and the reflected light is detected by a PD. The generated microwave signal is divided to two paths by an electrical coupler (EC1). One is amplified by an EA and fed to the PM as modulation signal. The other is sent to an electrical spectrum analyzer.

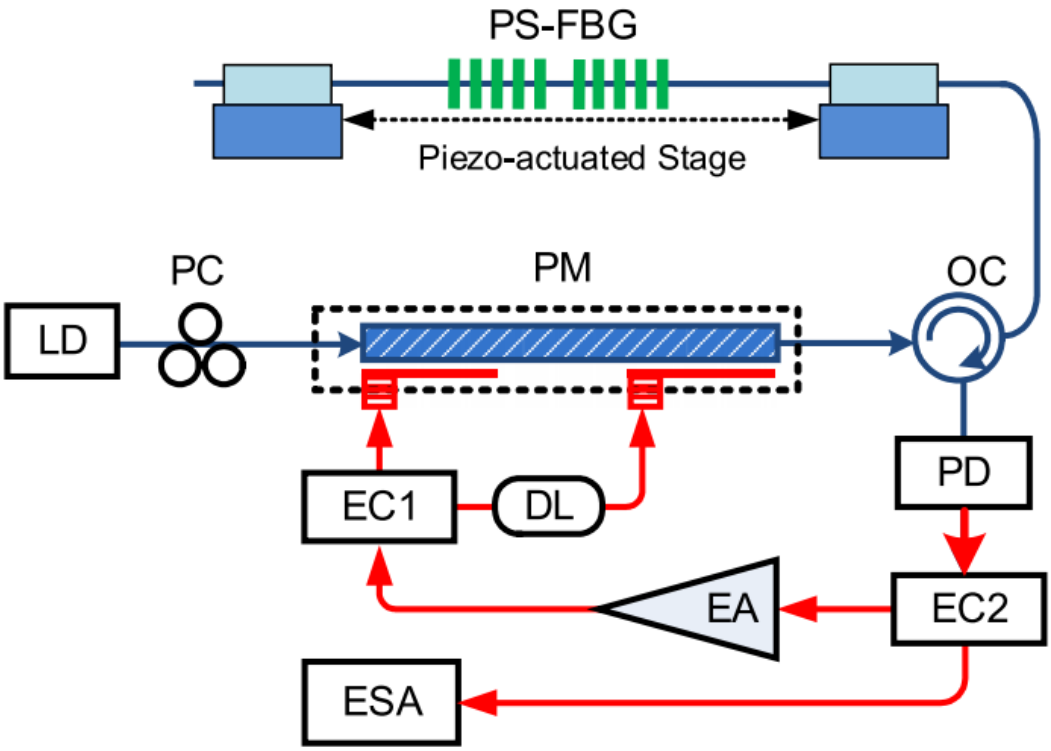

Fig. 2.20 Schematic diagram of an OEO for strain sensing. LD: laser diode; PC: polarization controller; PM: phase modulator; OC: optical circulator; PD: photodetector; EC: electrical coupler; EA: electrical amplifier; DL: delay line; ESA: electrical spectrum analyzer [113].

This OEO system provides an interrogation resolution of 450 KHz (3.60×10^{-6} nm), and a detection range of 10 GHz (0.08 nm) [113].

Although an OEO system provides a high speed and high resolution interrogation for optical sensors, it is only valid for the sensors as notch filters, such as PS-FBG. EAs with high 3-dB bandwidth are also very costly, which limits the detection range of the sensing system.

On the other hand, the time for scanning a full range of 50 GHz for a spectrum analyzer (Agilent E4448A) will be from 1 ms to 2000s, which is still low for the vibration sensing.

2.3.3 Interrogation in Time Domain

Utilizing WTT mapping can convert the wavelength shift of the optical sensors to a temporal shift of an electrical signal in the time domain, which can be interrogated by an oscilloscope with a high speed and high resolution.

Spectral shaping and wavelength-to-time (SS-WTT) mapping technique can be used for arbitrary microwave waveform generation, which can convert the spectrum of the spectral shaper to the profile of the generated waveform [39]. When the SS-WTT mapping technique is used to interrogate an FBG sensor, the wavelength shift of the FBG sensor can be converted to the time-shift of the generated waveform, which can be easily monitored by an oscilloscope. The schematic of a microwave waveform generation system based on SS-WTT technique is shown in Fig. 2.21. An ultrashort optical pulse generated by a pulse laser source is firstly spectrally shaped by an optical filter sensor. Then, the filtered optical pulse is sent to a dispersive element, which

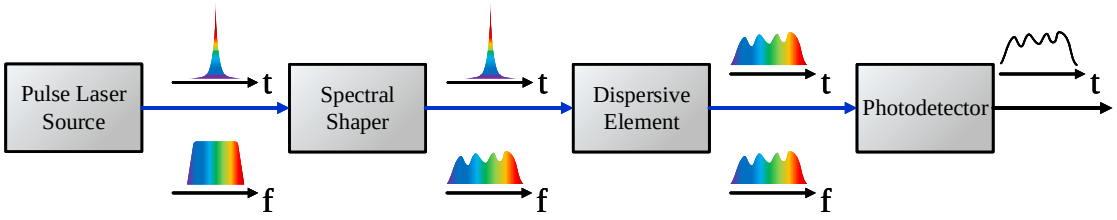

Fig. 2.21 Schematic of a microwave waveform generation based on spectral shaping and WTT mapping [39].

could be a length of dispersive fiber or a chirped FBG, to introduce a linear dispersion and perform linear WTT mapping. At the output of the PD, a microwave waveform with the shape identical to that of the filtered optical spectrum is generated. By monitoring the profile of the generated waveform, the transmission response of the optical filter sensor can be interrogated.

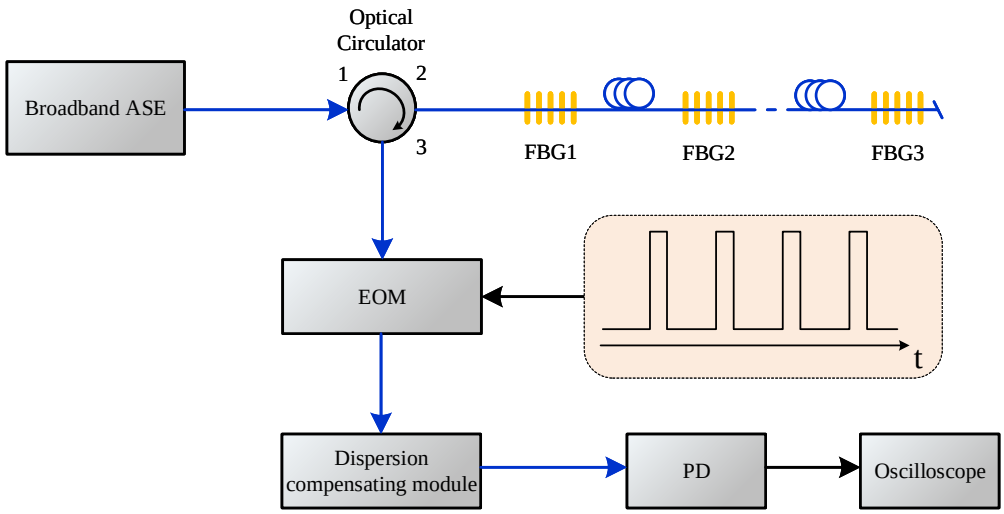

Fig. 2.22 Schematic diagram of a FBG sensor interrogation system based on SS-WTT mapping [114].

Fig. 2.22 shows a basic interrogation system of FBG sensors based on SS-WTT mapping technique [114]. In this system, an erbium-doped fiber amplified spontaneous emission (ASE)

source launches light into a FBG array via a circulator. The light, wavelength of which locates in the reflection spectrum of the FBG array, will be reflected and directed to an electro-optic modulator (EOM). The EOM is driven by a pulse generator. Then the pulsed signal is fed to a dispersion compensation module, where different wavelength components take different times to propagate. After that, a PD is used to get the optical signal. By measuring the time shift Δt, the wavelength shift $\Delta\lambda_B$ is revealed by the relation [114]:

$$\Delta\lambda_B = \Delta t / D \tag{2-13}$$

where D is the dispersion of the dispersion compensating module.

This system is simple and stable, providing an interrogation resolution of 12 pm, a detection range of 37.65 nm and an interrogation speed of 2.44 MHz. However, the width of the generated pulse is very large, leading to a low accuracy.

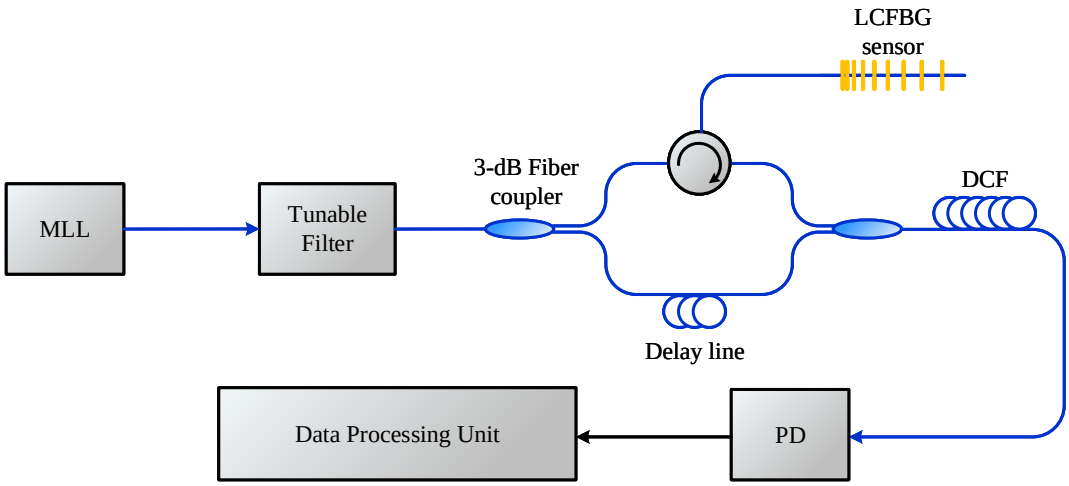

Fig. 2.23 Schematic diagram of a LCFBG sensor interrogation system based on SS-WTT mapping [42].

In order to reduce the generated electrical pulse, several structures have been proposed [42], [115]. Fig. 2.23 shows a LCFBG sensor interrogation system based on SS-WTT mapping [42]. Here, a MLL is used as a broadband light source. The light pulses are sent to a Mach-Zehnder interferometer (MZI) via a tunable optical filter, which is employed to control the temporal width of the pulse to the MZI. The MZI is constructed by a LCFBG sensor and a period of delay line, which acts as a spectrum shaper. At the output of the MZI, an optical spectrum with an increasing or decreasing FSR is generated, and the profile of the FSR would change if the wavelength of the LCFBG is shifted. A period of dispersion compensating fiber (DCF) is used to implement the WTT mapping. Then the light is fed to a PD, where a linearly chirped microwave waveform is obtained. A linearly chirped waveform is built as a reference, covering all possible bands of the generated microwave waveform. The correlation of the generated chirped microwave waveform with the reference waveform would provide a sharp correlation peak, and the peak position indicates the wavelength shift of the LCFBG. The experimental results show this system provides a resolution of 0.25 με at a speed of 48.6 MHz [42].

Using a linearly chirped microwave waveform as a modulation signal could also realize a WTT mapping for the optical notch filters, which is implied by adding different delays among different components of the spectrum by modulation.

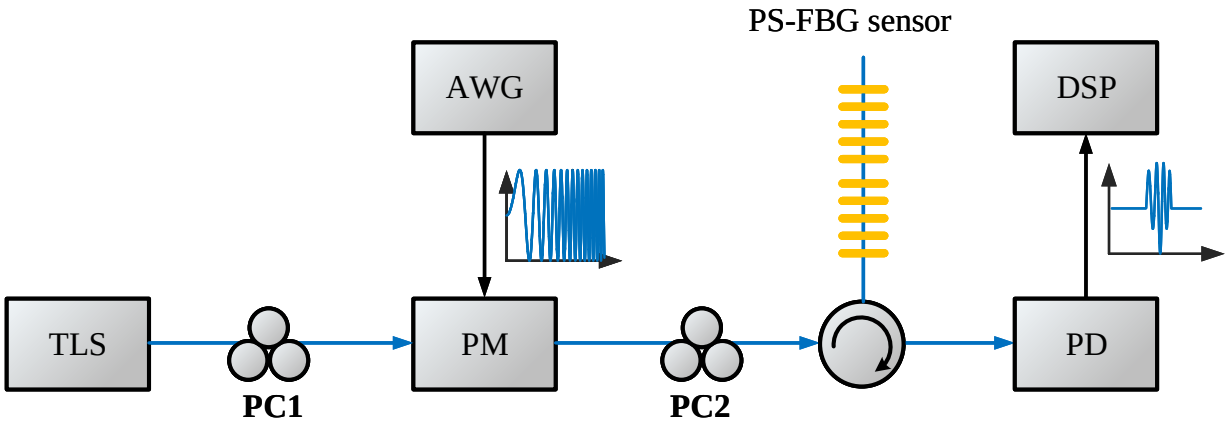

Fig. 2.24 Schematic diagram of a PSFBG sensor interrogation system based on WTT mapping [43].

Fig. 2.24 shows a PS-FBG sensor interrogation system based on WTT mapping [43]. In this system, a TLS, a PM, a PS-FBG and a PD construct a MPF, and an arbitrary waveform generator (AWG) is used to generate a broadband linearly chirped microwave waveform as a modulation signal. At the output of the PD, a filtered linearly chirped microwave waveform with a temporal profile identical to the shape of the frequency response of the MPF. When the wavelength of the PS-FBG shifts, the central frequency of the MPF would shift also, leading to a temporal and band shifts of the filtered linearly chirped waveform. By doing a cross-correlation between the filtered chirped microwave waveform with the AWG generated waveform, a sharp correlation peak would be obtained, and the peak position indicates the wavelength shift of the LCFBG. The system provides a resolution of 0.8 με at a speed of 1 MHz [43].

CHAPTER 3 INTERROGATION OF A STRAIN AND TEMPERATURE RANDOM GRATING SENSOR

Since a fiber grating sensor is sensitive to both strain and temperature changes, it is required that an interrogation system could discriminate the applied strain and temperature. A considerable number of discrimination methods have been proposed and demonstrated, such as adding a reference FBG, combining a LPG or building a FBG Fabry-Perot cavity. However, the extra components at the sensing parts increase the cost and complexity of the system.

In this chapter, we propose an approach to implement high-speed and high-resolution interrogation of a random grating sensor. The time domain interrogation leads to a high interrogation speed, while the pulse compression technique brings an improved interrogation resolution. Without using any interferometric structures, the system is simple and stable. Experimental results show that the proposed interrogation system can provide a stain and temperature resolution of 7.1 με and 0.79°C at an ultra-high speed of 20 MHz.

3.1 Operation Principle

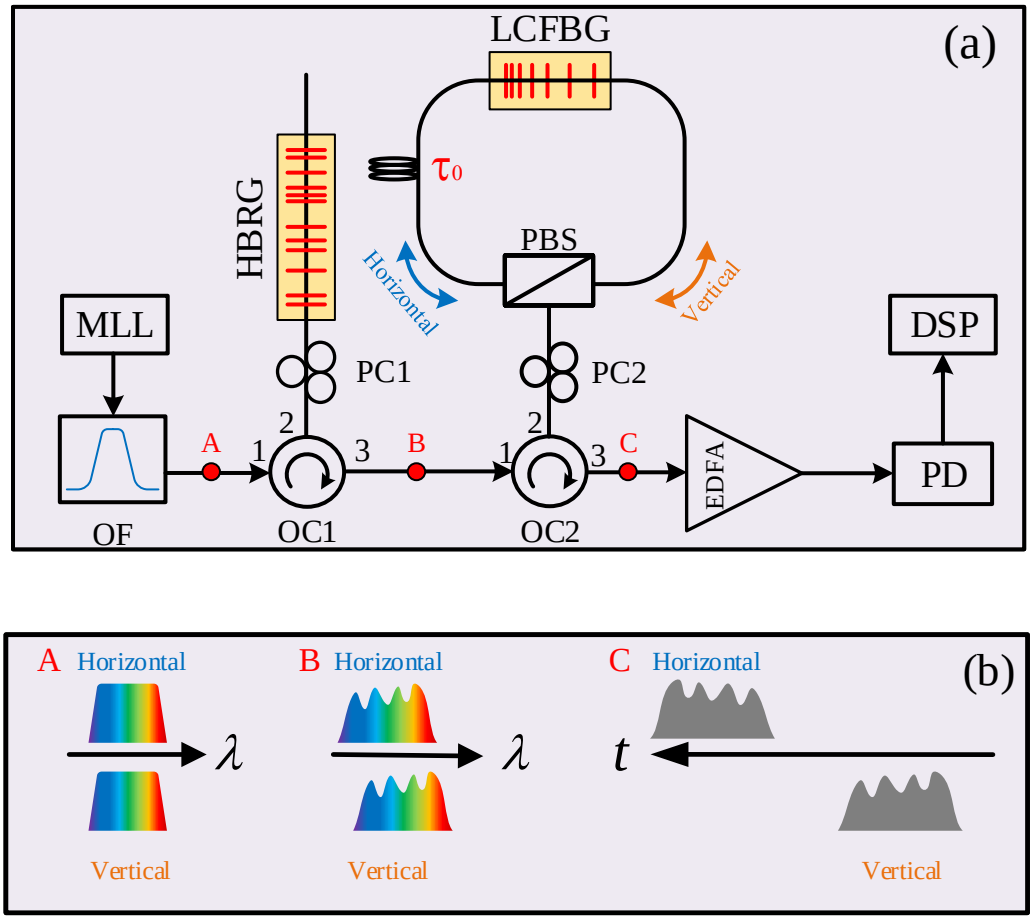

Fig. 3.1 (a) Schematic of the proposed HBRG sensor interrogation system; (b) the spectrums and temporal waveforms at different locations of the system. MLL: mode-locked laser; OF: optical filter; OC: optical circulator; PC: polarization controller; PBS: polarization beam splitter; EDFA: erbium-doped fiber amplifier; Hi-Bi random grating sensor: high-birefringence random grating sensor; PD: photo detector; DSP: digital signal processor.

The proposed interrogation system is shown in Fig. 3.1. An ultrashort optical pulse generated by a MLL is sent through a bandpass optical filter and an optical circulator (OC1) to an HBRG serving as a sensor. A polarization controller (PC1) is used to control the polarization direction of

the ultrashort pulse to have an angle of 45° relative to one principle axis of the HBRG. Thus, the incident light pulse is projected equally to the two principle axes of the HBRG. Two orthogonally polarized spectrums with a wavelength spacing determined by the birefringence of the HBRG are generated and sent to an optical loop via a second OC (OC2) and a second PC (PC2). The optical loop consists of a polarization beam splitter (PBS), an LCFBG, and a delay line. PC2 is used to align the polarization directions of the optical pulses (horizontal and vertical) with the principle axes of the PBS, so that one optical pulse with its polarization aligned with one principle axis (say, horizontal) is directed to the left path, and the optical pulse with its polarization aligned with the vertical principle axis of the PBS (vertical) is directed to the right path. Then, the horizontally polarized light is reflected from the shorter wavelength end of the LCFBG, thus wavelength-to-time mapping is implemented at the LCFBG with a positive dispersion coefficient. Meanwhile, the vertically polarized light is reflected from the longer wavelength end, and wavelength-to-time mapping with a negative dispersion coefficient is implemented. A section of single-mode fiber (SMF) is added to the left path to introduce an additional time delay, say τ_0 , thus the reflected horizontally polarized pulse would experience a $2\tau_0$ extra time delay, to make the two pulses further separated in the time domain to avoid overlap. The two mapped optical pulses are then amplified by an erbium-doped fiber amplifier (EDFA) before photodetection at a PD, and two electrical random waveforms are generated, corresponding to the two random spectrums of the HBRG sensor. By performing pulse compression using a DSP, the two pulses are significantly compressed, which leads to a precise measurement of the temporal shifts of the two random waveforms, leading to an accurate retrieval of the stain and temperature information.

A random grating is different from a regular Bragg grating. Instead of using a phase mask for a regular Bragg grating fabrication, a random grating is fabricated by using a femtosecond laser to spot-by-spot modify the refractive index of a fiber with the spot spacing randomly distributed [19]. The core-core mode Fabry-Pérot interferences and core-cladding mode Mach-Zehnder interferences existing in the fiber would generate irregular reflections. The superimposition of the irregular reflections would lead to a grating with random spectrum. The change of the environmental temperature and the applied strain will cause change in the interferometer length and effective refractive indices of the core mode and cladding modes, leading to a spectral shift in the corresponding reflection spectrum of the random grating. Mathematically, the wavelength shift can be expressed as

$$\Delta\lambda = g_1\Delta\varepsilon + g_2\Delta T \tag{3-1}$$

where $\Delta\varepsilon$ is the strain change, ΔT is the temperature change and g_1 g_2 are the corresponding coefficients, respectively.

Because the random spectrum is broad, direct interrogation of the spectrum shift using an OSA will have poor accuracy and low resolution. To increase the resolution, pulse compression technique can be employed. A random waveform can be compressed significantly by correlation [19]. If a shifted spectrum is correlated with a reference spectrum (a spectrum without experiencing a temperature or strain change), the correlation peak will appear at a location representing the spectrum shift. Thus, the shift of the spectrum can be accurately measured. However, the measurement of the spectrums using an OSA has a low speed. In the proposed approach, we

convert the spectrums to the time domain based on wavelength to time mapping, and the measurement can be done using a high-speed DSP.

As shown in Fig. 3.1, the LCFBG is employed to implement the WTT mapping. Assuming the value of the LCFBG introduced dispersion is $\ddot{\Phi}$ (ps/nm), for an input light pulse $g(t)$, the reflected light wave at the 3rd port of OC2 is given as [39]

$$y(t) = \exp\left(j \frac{t^2}{2\ddot{\Phi}_v} \right) \times G(\omega) \Big|_{\omega = \frac{t}{\ddot{\Phi}_v}} \tag{3-2}$$

where $G(\omega)$ is the Fourier transform of $g(t)$ and $\ddot{\Phi}_v$ (ps^2) is calculated by $\ddot{\Phi}_v = \frac{\lambda^2}{c} \ddot{\Phi}$.

From (3-2), it can be seen that the envelope of the LCFBG reflected light wave is proportional to the Fourier transform of the input light wave, which is the spectrum of the random grating. By applying the reflected optical pulse to a PD, an electrical random waveform is obtained. When a strain or temperature change is applied to the random grating, the wavelength shift will be translated to a temporal shift, given by,

$$\Delta T = \ddot{\Phi} \Delta \lambda \tag{3-3}$$

where $\Delta\lambda$ is the wavelength shift.

For a HBRG, the refractive indices of the fast axis and slow axis are different because of the birefringence of the fiber. Then, the (3-1) can be rewritten as

$$\begin{bmatrix} \Delta\lambda_f \\ \Delta\lambda_s \end{bmatrix} = \begin{bmatrix} g_{f1} & g_{f2} \\ g_{s1} & g_{s2} \end{bmatrix} \begin{bmatrix} \Delta\varepsilon \\ \Delta T \end{bmatrix} \tag{3-5}$$

where $\Delta\lambda_f$, g_{f1}, g_{f2} are the coefficients corresponding to $\Delta\lambda$, g_1, g_2 for the fast axis and $\Delta\lambda_s$, g_{s1}, g_{s2} are the coefficients corresponding to $\Delta\lambda$, g_1, g_2 for slow axis.

The relationship between the wavelength shifts and the strain and temperature is given by

$$\begin{bmatrix} \Delta\varepsilon \\ \Delta T \end{bmatrix} = \begin{bmatrix} g_{f1} & g_{f2} \\ g_{s1} & g_{s2} \end{bmatrix}^{-1} \begin{bmatrix} \Delta\lambda_f \\ \Delta\lambda_s \end{bmatrix} \tag{3-6}$$

As shown in Fig. 3.1, an optical pulse entering the optical loop will be split into two orthogonally polarized pulses, and the two pulses will experience complementary dispersion introduced by the LCFBG. Thus, the (3-3) can be rewritten as

$$\begin{bmatrix} \Delta T_x \\ \Delta T_y \end{bmatrix} = \begin{bmatrix} \ddot{\Phi} \\ -\ddot{\Phi} \end{bmatrix} \begin{bmatrix} \lambda_f \\ \lambda_s \end{bmatrix} \tag{3-7}$$

where $\Delta\tau_x, \Delta\tau_y$ are the time shifts of the correlation peaks for the horizontally and vertically polarized pulses, respectively.

Substitute (3-7) into (3-6), we finally get

$$\begin{bmatrix} \Delta\varepsilon \\ \Delta T \end{bmatrix} = \frac{1}{\ddot{\Phi}} \begin{bmatrix} g_{f1} & g_{f2} \\ g_{s1} & g_{s2} \end{bmatrix}^{-1} \begin{bmatrix} \Delta T_x \\ -\Delta T_y \end{bmatrix} \tag{3-7}$$

3.2 Experimental Results

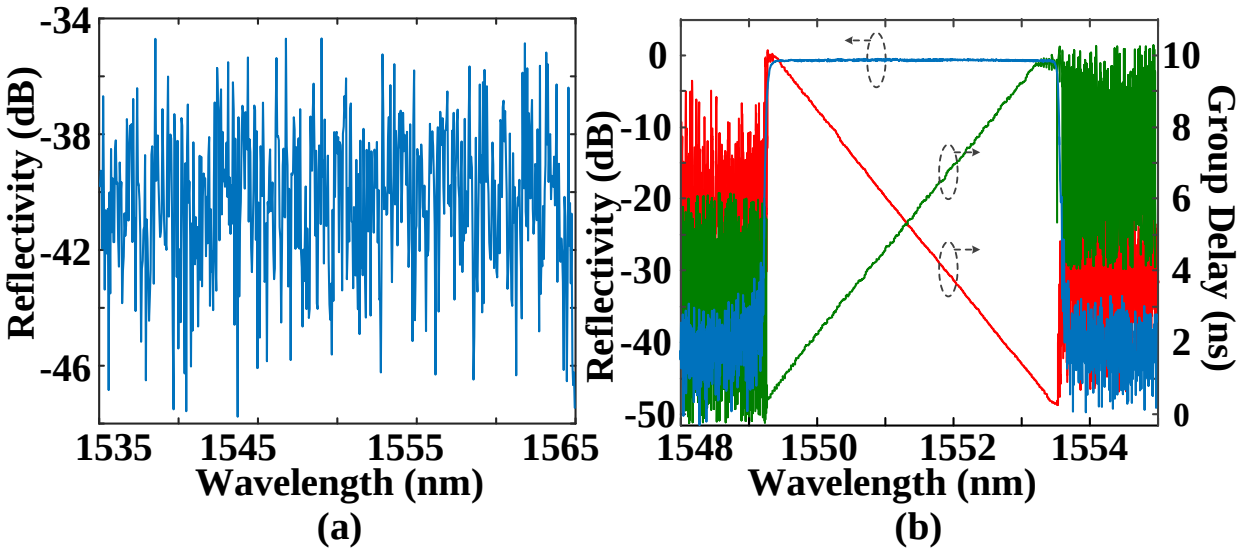

Fig. 3.2 (a)Reflection spectrums of the fabricated HBRG; (b) reflection spectrum and group delay responses of the LCFBG.

An experiment based on the setup shown in the Fig. 3.1 is performed. An ultrashort light pulse train with a repetition rate of 20 MHz generated by a tunable MLL (PriTel FFL-1550-20) with a 3-dB bandwidth of 8 nm and a pulse width of less than 600 fs is applied to a HBRG via a programmable bandpass optical filter (Waveshaper 4000S) and OC1. The random grating is fabricated in a PMF with a length of 50 mm. The reflection spectrum of the random grating is measured by a joint use of a tunable laser source (Yokogawa AQ2201) and an optical spectrum analyzer (Yokogawa AQ2201), as shown in Fig. 3.2(a). As can be seen, the random reflection spectrum over 30 nm is obtained.

Then an optical pulse reflected from the HBRG is sent to the optical loop, where the horizontally polarized optical pulse is directed by the PBS to the left path, and the vertically polarized optical pulse is directed to the right path. The optical pulses are then experiencing WTT mapping at the LCFBG. The LCFBG used in the experiment is fabricated in a SMF with a length of 1 m. Its reflection spectrum is measured by an optical vector analyzer (OVA, Luna Technologies) and is shown in Fig. 3.2(b). As can be seen, the LCFBG has a bandwidth of 4 nm and a central wavelength of 1551.4 nm. The group delay responses measured from its short and long wavelength ends are also shown in Fig. 3.2(b). It can be seen that two group delay responses are complementary and the dispersion coefficients are +2500 ps/nm and -2500 ps/nm, respectively. The central wavelength of the ultrashort light pulse is tuned at 1551.4 nm, which is identical to the central wavelength of the LCFBG, and the bandwidth of the optical filter is set as 3 nm, to get a higher optical power density for effective photodetection. Thus, the pulse width of the generated waveform should be 7.5 ns. The repetition rate of the pulse train is 20 MHz. To avoid overlap between the two reflected pulses, the time delay τ_0 introduced by the delay line in the optical loop should be greater than 7.5 ns and smaller than 35 ns. After amplified by an EDFA, the optical pulses after WTT mapping are fed into a PD (Newport, model 1014, 45 GHz) and the generated electrical waveforms are monitored by a real-time oscilloscope (Keysight, DSOZ504A, 50 GHz bandwidth, 160 GSa/s). Fig. 3.3(a) shows the generated electrical waveforms, from which we could see that the pulse widths are around 7.5 ns. Fig. 3.3(b), (c) and (d) shows the auto-correlation of the waveform from the horizontal polarization direction, cross-correlation between the waveforms from the two directions and the auto-correlation of the waveform from the vertical polarization direction, respectively. As can be seen, the pulses are significantly compressed for auto-correlation, and no correlation peak is observed for cross-correlation. The results confirm that

a random waveform can be significantly compressed for auto- correlation, and no compression is obtained for cross-correlation since the two waveforms used for cross-correlation are different due to the complementary wavelength-to-time mapping.

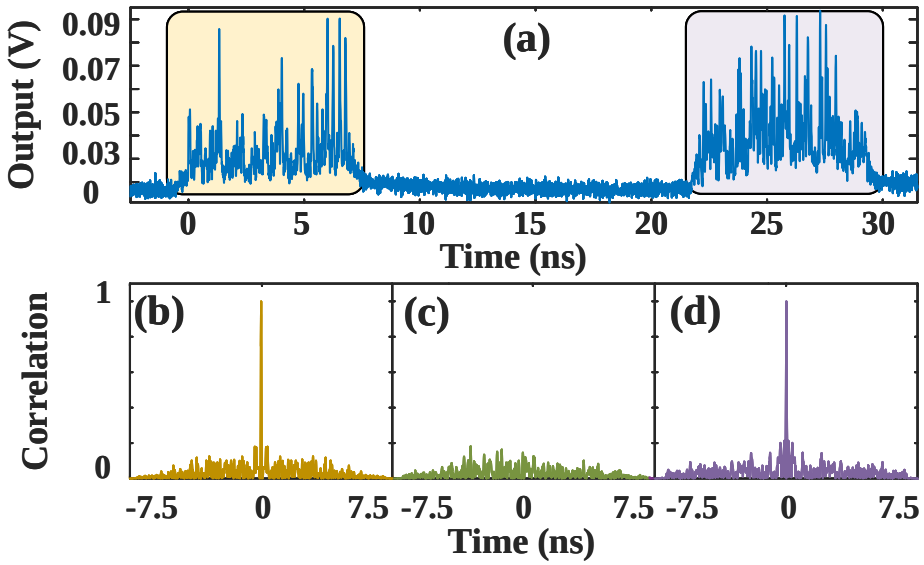

Fig. 3.3 (a) Generated random waveforms, (b) auto-correlation of the waveform from the horizontal direction, (c) cross-correlation between the waveforms from the two directions, and (d) auto-correlation of the waveform from the vertical direction.

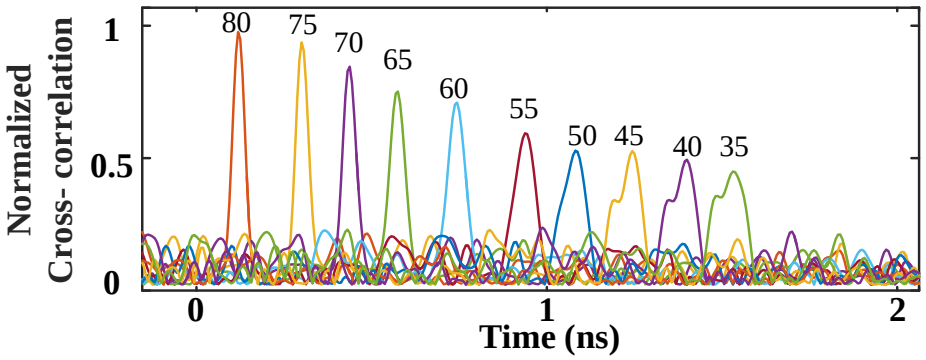

Fig. 3.4 Compressed pulses from x-axis when different temperature is applied to the random

grating sensor. The reference is the waveform generated at 82 °C.

Fig. 3.4 shows the compressed pulses from the horizontal direction when a different temperature is applied to the HBRG sensor while maintaining the strain constant. The reference waveform is one generated at 82 °C. As can be seen the time shift is increasing when the temperature is reducing. This is because the reference waveform is taken at 82 °C.

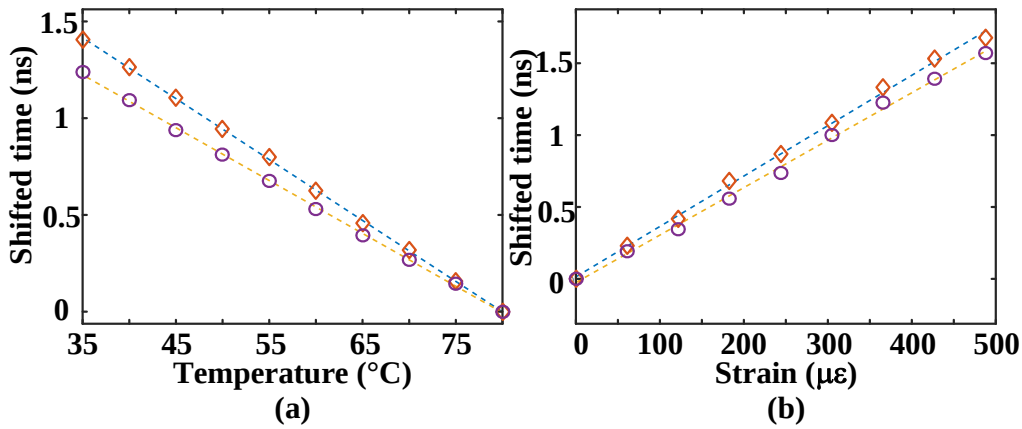

Fig. 3.5 Experimental results. (a) Time shifts of the peaks versus the temperature with no strain applied; (b) time shifts of the peaks versus an applied strain at room temperature (23.2°C). The circles and diamond indicate the experimental data corresponding to time shifts of the correlation peaks.

Fig. 3.5(a) shows the time shifts of the compressed pulses versus temperature change with no strain applied, and Fig. 3.5(b) shows the time shifts of the compressed peaks pulses versus strain change at a fixed room temperature (23.2 °C). Based on the measurements in Fig. 3.5, we get the relationship between the strain and temperature and the time shifts, which condition number is 212.

$$\begin{bmatrix} \Delta T \\ \Delta \varepsilon \end{bmatrix} = \begin{bmatrix} 0.3976\ \mu\varepsilon / \text{ps} & -0.4217\ \mu\varepsilon / \text{ps} \\ -3.2908\ ^{\circ}C / \text{ps} & 3.7932\ ^{\circ}C / \text{ps} \end{bmatrix} \begin{bmatrix} \Delta\tau_x \\ \Delta\tau_y \end{bmatrix} \tag{3-9}$$

As can be seen, for this particular system, once the time intervals are measured, the strain and the temperate can be simultaneous estimated.

Based on Fig. 3.5, the sensitivities are 31.48 ps/°C and 3.5 ps/με, which can be further improved when an LCFBG with greater dispersion coefficient is used. The minimum width of the compressed pulses is 25 ps, corresponding to a temperature resolution of 0.79 °C and strain resolution of 7.1 με, which can be also improved when an LCFBG with greater dispersion is employed. The experimental errors are within ±0.8°C and ±9 με. Comparing with the results reported in [9], this system shows a higher sensitivity and higher accuracy. Without using an interferometric structure, the system is ultra-stable. The interrogation speed is determined by the repetition rate of the MLL, which is 20 MHz.

3.3 Summary

In this chapter, we have proposed and experimentally demonstrated an approach to implement high-speed and high-resolution interrogation of a HBRG sensor based on spectral shaping and wavelength-to-time mapping for simultaneous measurement of strain and temperature. The key contribution of the work was the use of a HBRG to generate a random spectrum, which was compressed in the time domain after wavelength-to-time mapping. Since the spectrums were converted to the time domain, high speed and high resolution integration using a DSP is possible. The approach was verified experimentally. simultaneous measurements of stain and temperature with a resolution of 7.1 με and 0.79°C at an ultra-high speed of 20 MHz was demonstrated.

CHAPTER 4 TEMPERATURE AND REFRACTIVE INDEX SILICON PHOTONIC MICRODISK SENSOR

Reflective index sensing is another attracting area in civil engineering. Traditional optical fiber sensors are insensitive to the environmental refractive index. Coating metal or other materials over the fiber cladding or fiber core could be a solution, but the cost and complexity of the system are increased significantly, while the provided sensitivity is still limited. Silicon photonic resonator sensors, which has a high sensitivity to the reflective index changing, shows a promising future.

In this chapter, an interrogation system for a MDR sensor is proposed and experimentally demonstrated, with a high speed and high resolution. The sensing information is converted to time domain, which ensure the high interrogation speed. By using two phase-only matched filters with windowing technique, the noises can be attenuated significantly. Thus, the sensing information can be revealed with a high resolution. Again, without using any optical interferometer structure, the system is ultra stable. The experimental results show that the sensor has a sensitivity of 3.07 μs/℃ and a resolution of 0.234℃ as a temperature sensor, and a sensitivity of 1.3 ms/RIU and a resolution of 1.32×10^{-3} RIU as an refractive index sensor. The interrogation speed is as high as 100 kHz

4.1 Operation Principle

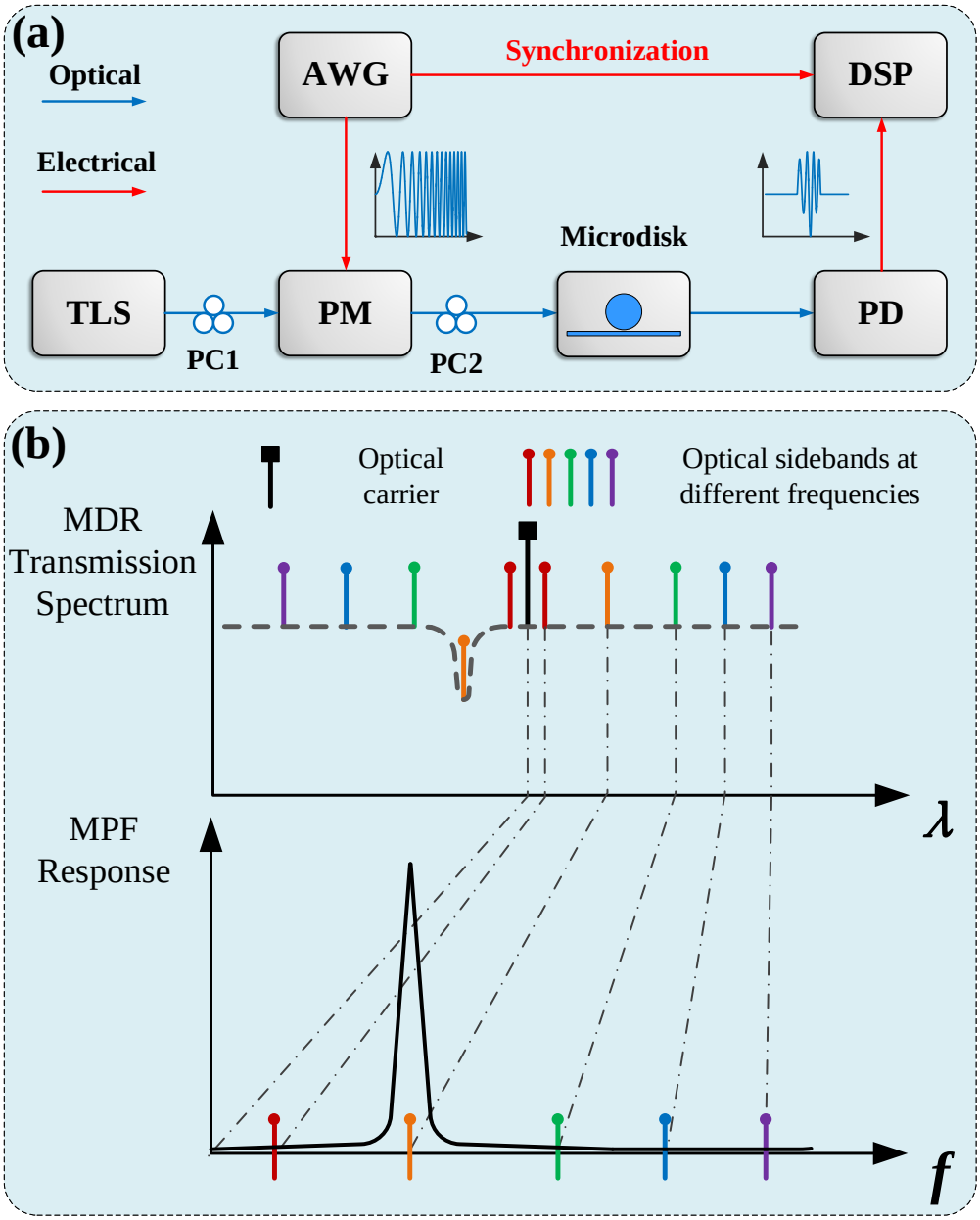

Fig. 4.1 (a) The configuration of the proposed interrogation system; (b) An MPF based on phase modulation to intensity modulation conversion. LD: laser diode; PC: polarization controller; PM: phase modulator; PD: photo detector; AWG: arbitrary waveform generator; DSP: digital signal processor.

Fig. 4.1(a) shows the configuration of the proposed interrogation system for temperature and RI sensing using a silicon photonic MDR sensor. It consists of a laser diode (LD), two PCs (PC1 and PC2), a PM, an MDR, and a PD. A light wave generated by the LD is sent to the PM. The polarization direction of the incident light wave is aligned with the principle axis of the PM by PC1. The phase-modulated signal at the output of the PM is introduced to the on-chip MDR via PC2, which is used to ensure only the TE mode is excited in the waveguide. By filtering out one sideband of the phase-modulated signal by the notch of the MDR, PM-IM conversion is performed, and a microwave signal is recovered at the PD. The overall operation is equivalent to an MPF with the center frequency of the passband equal to the wavelength difference between the optical carrier and the resonant wavelength of the MDR, as shown in Fig. 4.1(b). A broadband LCMW generated by an AWG is fed to the MPF. At the output of the MPF, a filtered microwave waveform with the central frequency determined by the passband of the MPF is obtained. The location of the filtered microwave waveform is determined by the central frequency of the MPF, thus by estimating the temporal location of the filtered microwave waveform, the wavelength shift of the MDR is obtained, which is an indicator of the temperature or RI change.

The resonant wavelength of a MDR is calculated by (2-5), and the wavelength responses for cladding refractive index and temperature are shown in (2-6) and (2-7) respectively. Assuming the wavelength of the optical carrier is λ_c, the central frequency of the MPF, which is given by (2-11), could be rewritten as

$$f_{MPF} \approx \left(\frac{c}{n_{avg}} \right) \times \left| \frac{\lambda_c - \lambda_{res}}{\lambda_c^2} \right| \tag{4-1}$$

where *c* is the velocity of light in vacuum, n_{avg} is the average refractive index for the optical path consisting of fibers and the silicon waveguides When the resonate wavelength of the MDR shifts, the central frequency of the MPF will change. The frequency change can be expressed as

$$\Delta f_{MPF} = K\Delta\lambda_{res} \tag{4-2}$$

where $K = c/\left(n\lambda_c^2\right)$ and $\Delta\lambda_{res}$ is the wavelength shift ($\Delta\lambda_{Temp}$ or $\Delta\lambda_{RI}$).

Mathematically, for a LCMW, the instantaneous frequency of the waveform is given by

$$f\left(t\right) = f_0 + Ct \tag{4-3}$$

where C is the chirp rate, f_0 is the initial frequency, and *t* is the time. When a LCMW is fed to an MPF, the temporal location of the output waveform is calculated by $t = \left(f_{MPF} - f_0\right)/C$. The relationship between the wavelength shift of the MDR and the temporal location is given by

$$\Delta T = \frac{K}{C}\Delta\lambda_{res} \tag{4-4}$$

When the temporal location is measured, using (4-4) with (2-6) or (2-7), the temperature change or refractive index change can be revealed.

The interrogation resolution is limited by the 3-dB bandwidth of the MPF, which determines the spectral width of the filtered microwave waveform. To reduce the bandwidth of the MFP, the Q factor of the MDR should be increased. To do so, we add a slab waveguide surrounding the disk and the bus waveguide, to reduce the loss due to sidewall roughness. The 3D view and the cross-

sectional view of the MDR are shown in Fig. 4.2(a). The radius of the microdisk is 3.7 μm, and the width of the bus waveguide is 520 nm. A slab waveguide with a height of 60 nm is added surrounding the disk and the bus waveguides. To increase the sensitivity, a direct contact between the MDR sensor and a solution for which its refractive index is to be measured is needed. To do so, the silica cladding is removed. Fig. 4.2(b) shows the simulated fundamental mode profile in a conventional MDR, and Fig. 4.2(c) shows the fundamental mode profile in the proposed MDR. Comparing the two mode profiles, it can be clearly seen that the interaction between the light field and the sidewalls of the proposed MDR is weakened. Thus, the scattering due to sidewall roughness is reduced and a higher Q factor is ensured.

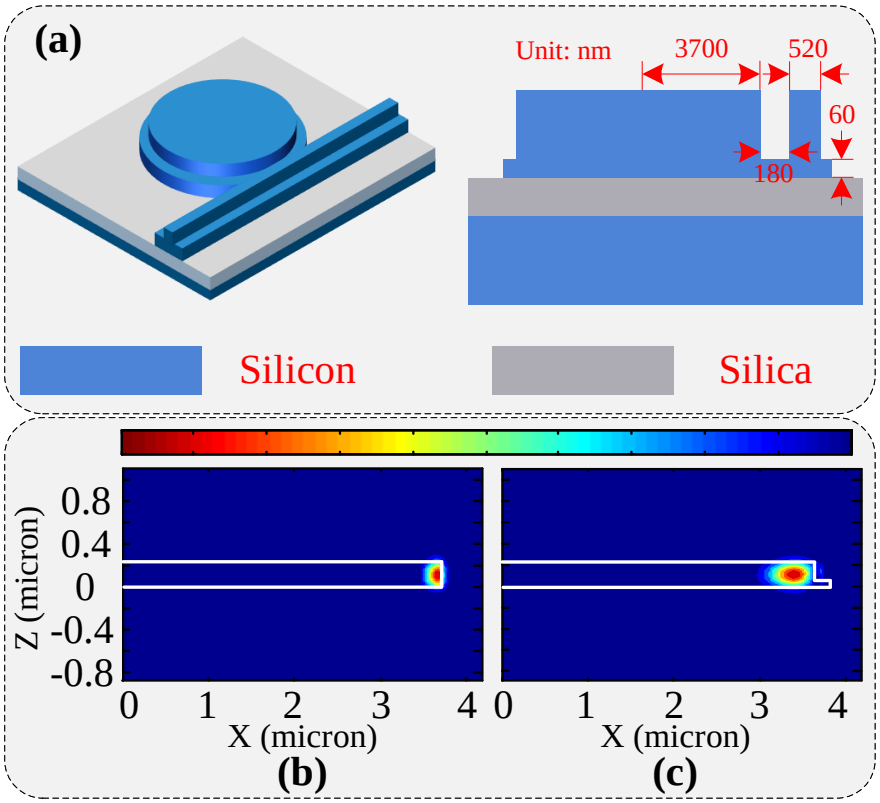

Fig. 4.2 (a) 3-D view and cross-sectional view of the proposed MDR; (b) simulated fundamental TE0 profile of a conventional MDR; (c) simulated fundamental TE0 profile of the proposed MDR.

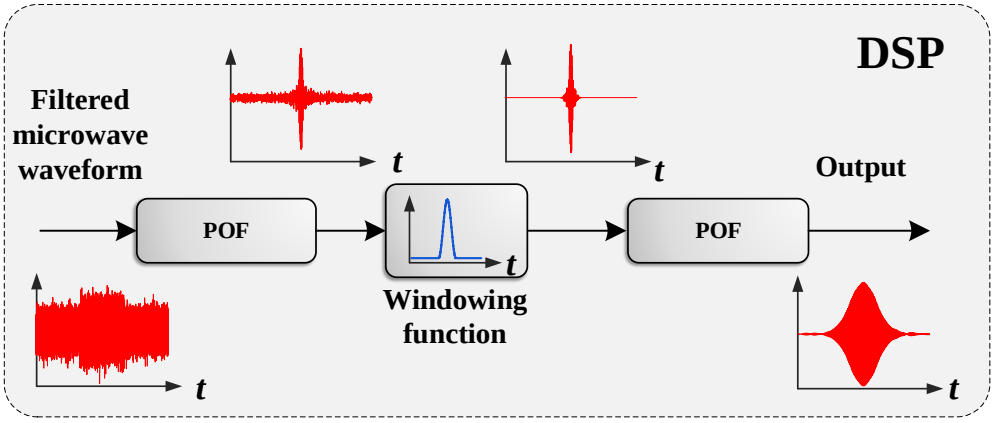

Fig. 4.3 DSP process for improving the SNR of the generated signal.

The detection accuracy is affected by the noise of the filtered microwave waveform [33]. Due to a high insertion loss of the system, the filtered microwave waveform is weak with a poor SNR. To increase the SNR to ensure an accurate measurement of the time shift, the filtered microwave waveform is filtered using a DSP. The signal processing procedure is shown in Fig. 4.3. A POF based on the reference LCMW is built which is correlated with the filtered microwave waveform, thus the microwave waveform is compressed. On the other hand, since the noise is not correlated with the LCMW, its distribution after phase-only filtering is not changed. Thus, by applying a windowing function to select the compressed pulse, the noise is significantly suppressed. Finally, by re-correlating the noise-suppressed compressed pulse with the POF, a microwave waveform with an increased SNR is obtained.

Mathematically, the filtered microwave waveform at the output of the PD can be expressed as

$$x(t) = s(t) + n(t) \tag{4-5}$$

where $s(t)$ is the filtered microwave waveform and $n(t)$ is the noise.

We use the LCWM, denoted as $r(t)$, generated by the AWG as a reference to build a POF. Considering the spectrum of the reference is $R(j\omega)$, the spectrum response of the POF is $\frac{R(j\omega)}{|R(j\omega)|}$. So, the compressed pulse is given by

$$\begin{aligned} Y_1(t) &= F^{-1}\left[X(j\omega) \times \frac{R^* j(\omega)}{|R(j\omega)|} \right] \\ &= F^{-1}\left\{ \left[S(j\omega) + N(j\omega) \right] \times e^{-j\phi_R(j\omega)} \right\} \\ &= F^{-1}\left[|S(j\omega)| e^{j\phi_s(j\omega)} \times e^{-j\phi_R(j\omega)} + |N(\omega)| e^{j\phi_n(j\omega)} e^{-j\phi(j\omega)} \right] \end{aligned} \tag{4-6}$$

where $R^*(j\omega)$ is the complex conjugate of $R(j\omega)$, $X(j\omega)$, $S(j\omega)$ and $N(j\omega)$ are the Fourier transforms of $x(t)$, $s(t)$ and $n(t)$, respectively, and $\phi_s(j\omega)$, $\phi_n(j\omega)$ and $\phi_R(j\omega)$ are the phase terms of $S(j\omega)$, $N(j\omega)$ and $R(j\omega)$, respectively.

Because the filtered microwave waveform is from the reference LCMW and the MPF has a linear phase response, we have $\phi_s(j\omega) = \phi_R(j\omega)$. Thus, (4-6) is simplified to be

$$\begin{aligned} Y_1(t) &= F^{-1}\left[|S(j\omega)| e^{j\phi_s(j\omega)} \times e^{-j\phi_R(j\omega)} + |N(j\omega)| e^{j\phi_n(j\omega)} e^{-j\phi_R(j\omega)} \right] \\ &= F^{-1}\left[|S(j\omega)| + |N(j\omega)| e^{j\phi_n(j\omega)} e^{-j\phi_R(j\omega)} \right] \end{aligned} \tag{4-7}$$

From (4-7), we can see that the filtered microwave waveform is compressed. Since the phase of the noise is randomly distributed and it is not cancelled by the phase term from the POF during the correlation process, the noise is not compressed. By applying a windowing function to select the compressed pulse, the noise would be significantly suppressed. Then, by re-correlating the

compressed pulse with the POF, the microwave waveform is recovered, but with significantly increased SNR.

$$\begin{aligned} Y_2(t) &= F^{-1}\left[\left(\left|S(j\omega)\right|+\left|N'(j\omega)\right|e^{j\phi_n(j\omega)}e^{-j\phi_R(j\omega)}\right)\times\frac{R^*(j\omega)}{\left|R(j\omega)\right|}\right] \\ &= F^{-1}\left[\left|S(j\omega)\right|e^{-j\phi_R(j\omega)}+\left|N'(j\omega)\right|e^{j\phi_n(j\omega)}e^{-j2\phi_R(j\omega)}\right] \end{aligned} \tag{4-8}$$

where $N'(\omega)$ is the spectrum of the filtered noise after windowing.

From (4-8), it can be seen that the microwave waveform after signal processing is a time reversed version of the microwave waveform at the output of the PD, but the noise is significantly suppressed. Thus, the filtered microwave waveform is rebuilt with an improved SNR.

The bandwidth of the filtered microwave waveform is determined by the bandwidth of the MDR, given by

$$B = K\frac{\lambda_{res}}{Q} \tag{4-9}$$

where Q is the quality factor and $K = c/\left(n\lambda_c^2\right)$. The time bandwidth product (TBWP) of the filtered microwave waveform is

$$TBWP = \frac{K^2\lambda_{res}^2}{Q^2C} \tag{4-10}$$

At the output of the first POF, the temporal duration of the filtered microwave waveform is compressed by *TBWP* times. Since the noise after the POF is still uniformly distributed, if a Hamming window with a 3-dB bandwidth equal to the width of the compressed waveform is

applied, the microwave waveform is not affected, but the noise is significantly reduced by *TBWP* times. Thus, the SNR of the filtered microwave waveform is increased by $10\log_{10}(TBWP)$ dB. For example, if the *TBWP* is 1000, the SNR is increased by 30 dB.

A numerical simulation using Matlab is implemented, as shown in Fig. 4.4. A perfect broadband LCWM is generated, shown in Fig. 4.4(a), and two parts of it are selected out, shown in Fig. 4.4(b). Doing the data processing described above, the result is shown in Fig. 4.4(c), from which we can see that the selected LCMWs is recovered with a windowing response. Adding a Gaussian random noise on the previous selected LCMWs, which maximum amplitude is 10 times higher than the signal, as shown in Fig. 4.4(d), and doing the processing again, the result is shown in Fig. 4.3(e), with a significantly improved SNR. Comparing Fig. 4.4(e) with Fig. 4.4(c), we could see that the selected signal is slightly degenerated, while the central time locations are maintained.

By using this method, the filtered LCMW can be recovered and the noises is significantly suppressed, leading to a highly improved SNR. Working with digital electronics with an ultra-high speed and resolution for the measurement, the resolution of the interrogation system is highly elevated.

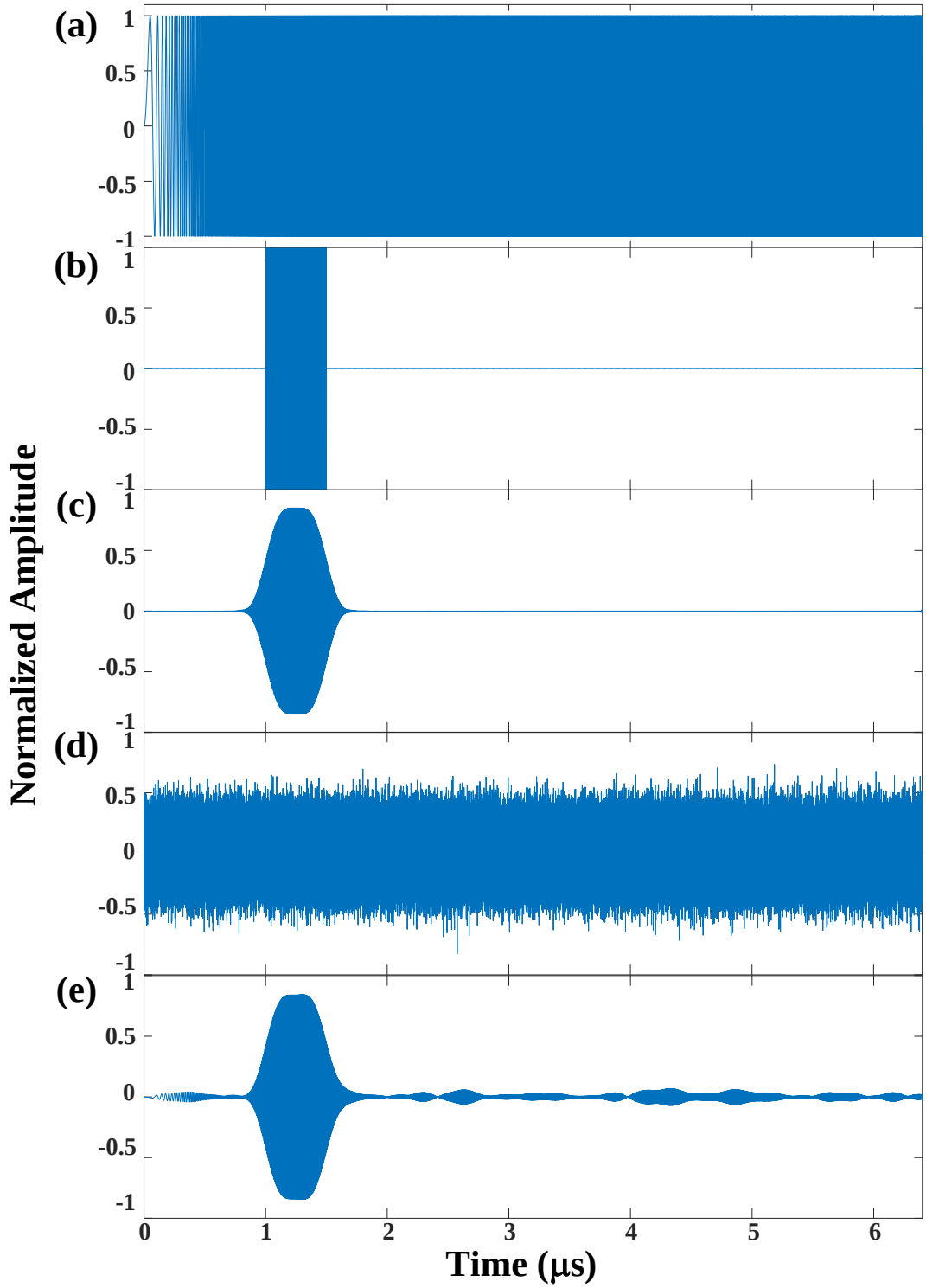

Fig. 4.4 (a) Generated perfect LCMW; (b) filtered LCMW; (c) processed LCMW based on (b); (d) filtered LCMW with a strong noise; (e) processed LCMW based on (d).

4.2 Experimental Results

An experiment based on the setup shown in Fig. 41(a) is performed. A CW light from a TLS (Anritsu, MG9638A) is sent to the PM (Thorlabs, 40 GHz) via PC1, and phase modulated by a broadband LCMW, which is generated by an AWG (Keysight M8195A). Then, the modulated light wave is introduced to the MDR, where the 1st order sideband is eliminated and PM-IM conversion is performed. At the output of the MDR, the optical carrier and the other 1st order sideband are sent to the PD (Newport, model 1014, 45 GHz). A filtered microwave waveform is generated at the output of the PD, which is sent to a DSP for signal processing.

The key device in the system is the silicon photonic MDR, which is fabricated using CMOS-compatible technology with 193-nm optical projection lithography. Fig. 4.5(a) shows the SEM micrographs of the fabricated MDR. An OVA (LUNA OVA 5000) is used to evaluate the optical performance of the fabricated MDR. Fig. 4.5(b) shows the spectrum of the MDR. Fig. 4.5(c) gives a zoom-in view of a TE_0 mode resonance. As can be seen, the free spectral range (FSR) of the MDR is 30.05 nm, and the 3-dB bandwidth is around 9 pm. The Q factor of the fabricated MDR is calculated to be 172,400, which is much higher than a conventional MDR [31], ensuring an improved interrogation resolution.

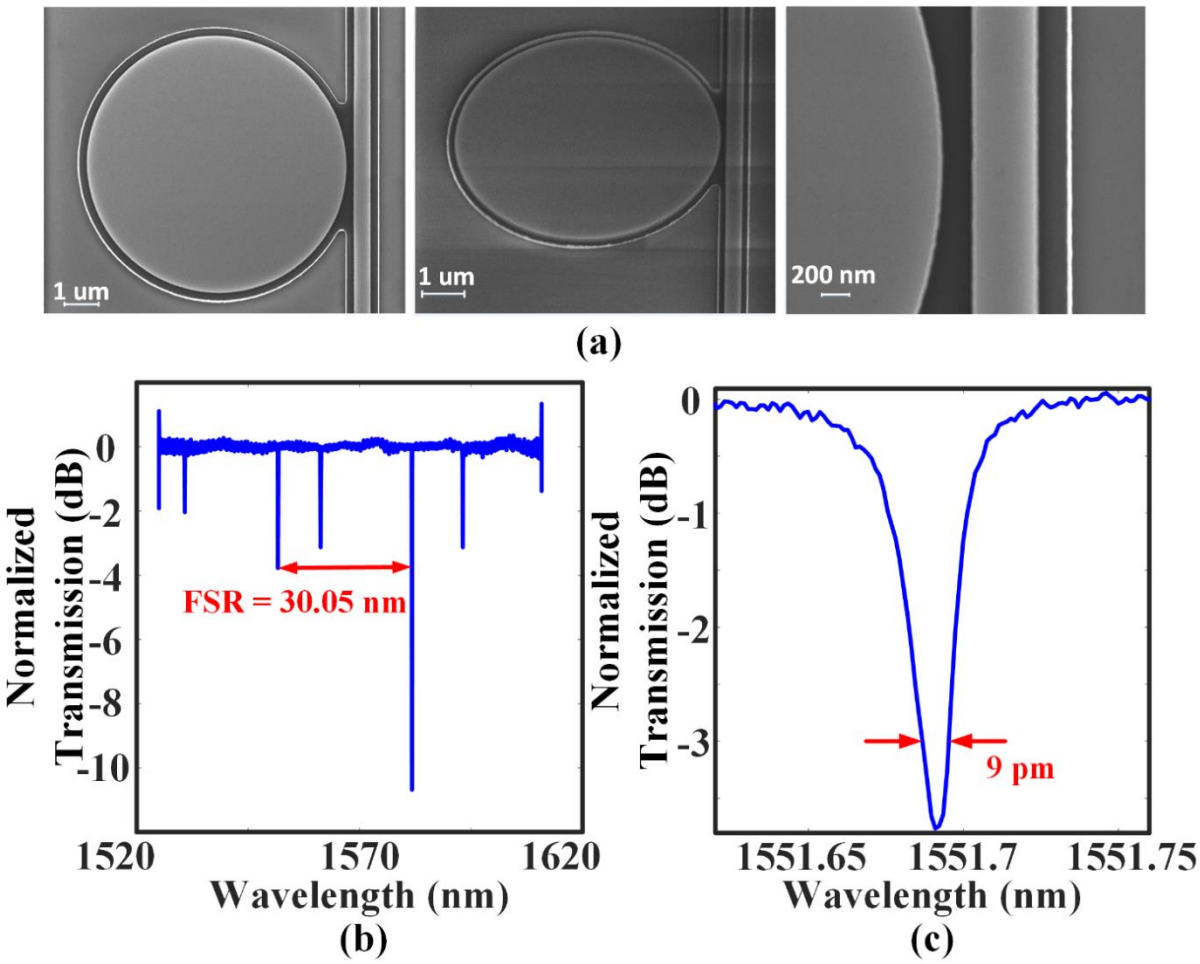

Fig. 4.5 (a) SEM micrographs of the fabricated microdisk; (b) normalized transmission spectrum of the fabricated microdisk with air cladding; (c) zoom-in view of the TE0 mode resonance of the fabricated microdisk with air cladding.

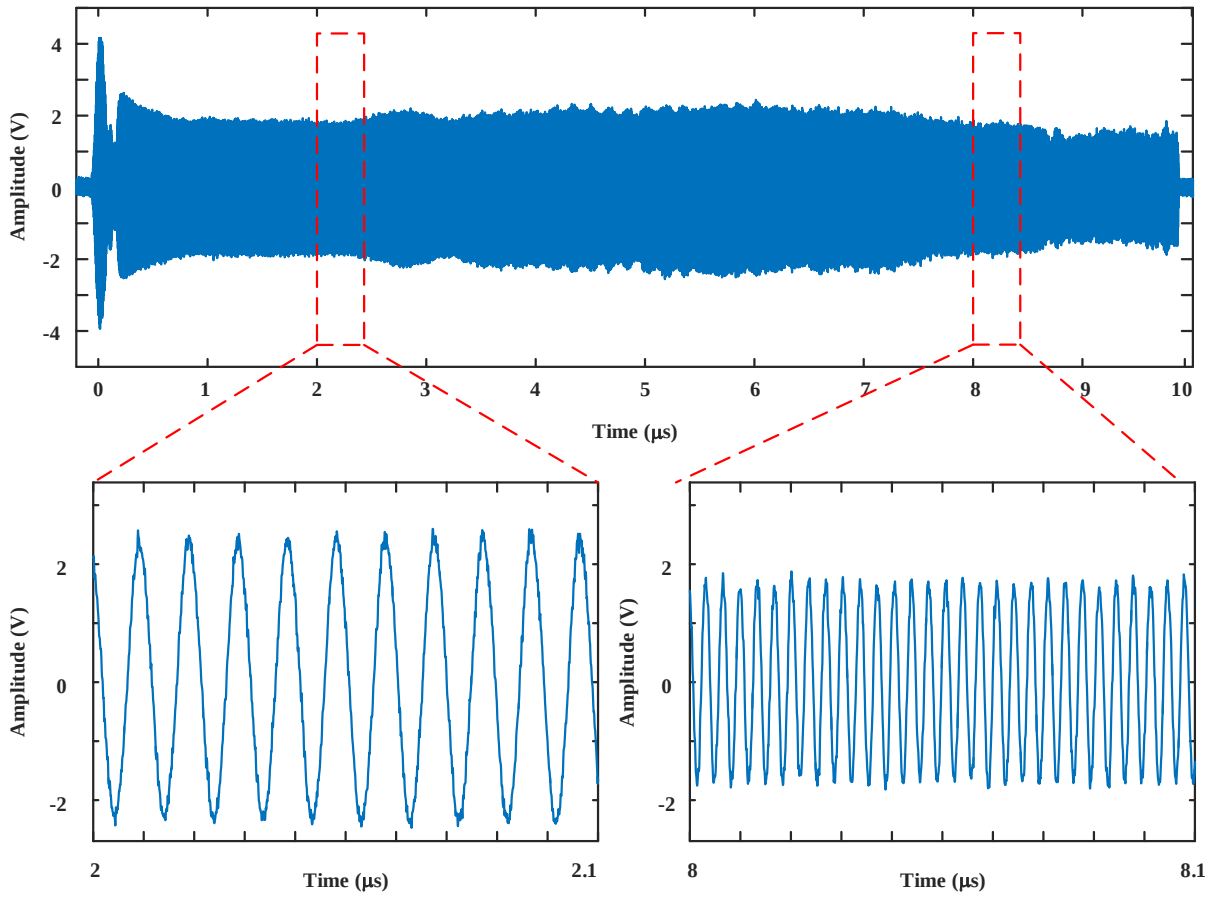

Fig. 4.6 Broadband LCMW generated by an AWG

Firstly, the resonant wavelength shift with the temperature change is investigated. The wavelength of the optical carrier is set as 1552.27 nm, and an LCMW with a temporal duration of 10 μs and a chirp rate of 3.2 GHz/ μs is generated by the AWG as the modulation signal, as shown in Fig. 4.6. Fig. 4.7(a) and 4.7(b) shows two filtered microwave waveforms at two different temperatures at the output of the PD. As can be seen, the filtered microwave waveforms are separated in the time domain, with the temporal separation corresponding to the wavelength change of the MDR. The time width of a filtered microwave waveform is around 700 ns. Since the microwave waveforms are very noisy, an accurate estimation of the temporal location of the

filtered microwave waveform is difficult. A solution is to remove the noise, which can be performed by matched filtering in a DSP. Fig. 4.7(c) shows a compressed microwave pulse which is done by correlating the filtered microwave waveform with a POF built from the LCMW. Thanks to the large TBWP of the filtered microwave waveform, the width of the compressed pulse after the POF is around only 0.4 ns, with a compression ratio of 1758. Applying a Hamming window to the compressed pulse with a width of 0.7 ns and feeding it to the POF again, the microwave waveform is recovered and the noise is significantly attenuated.

Fig. 4.7(d) and (e) show the processed waveforms corresponding to those shown in Fig. 4.7(a) and (b), respectively. Since the noise is significantly suppressed, the temporal location of the microwave waveform can be easily estimated. Fig. 4.8(a) shows estimated temporal locations vs. temperature change. As can be seen the sensitivity for temperature measurement is 3.07 μs/℃, corresponding to 76.8 pm/℃. Because of the imperfect optical phase response of the MDR, the measured 3-dB bandwidth of the MPF is larger than the bandwidth of the MDR, which is 2.25 GHz. Thus, the corresponding sensing resolution is 0.234℃.

Then, the resonant wavelength shift with the refractive index change is investigated. Setting a temperature at 23.4 ℃ and the wavelength of the light carrier at 1558.35 nm, and change in the cladding with different NaCl solutions is measured. Fig. 4.8(b) shows the estimated temporal locations vs. cladding refractive index change by change the NaCl solutions with different refractive indexes. From the fitted line, it can be seen that the sensitivity for cladding RI measurement is 1.3 ms/RIU, corresponding to 33.28 nm/RIU. The measured 3-dB bandwidth of the MPF is 5.5 GHz, thus the corresponding sensing resolution is 1.32×10^{-3} RIU.

Note that the change of the cladding refractive index of the cladding is significant, the resonant wavelength has a large shift. As shown in Fig. 4.9(a), when the MDR is with water cladding, the resonant wavelength is shifted to 1558.59 nm, a net shift of 6.99 nm. From the zoom-in view shown in Fig. 4.9(b), it can be noticed that the 3-dB bandwidth is increased to around 39 pm and the Q factor is reduced to 40000, which is due to the change in coupling coefficient between the bus and the microdisk.

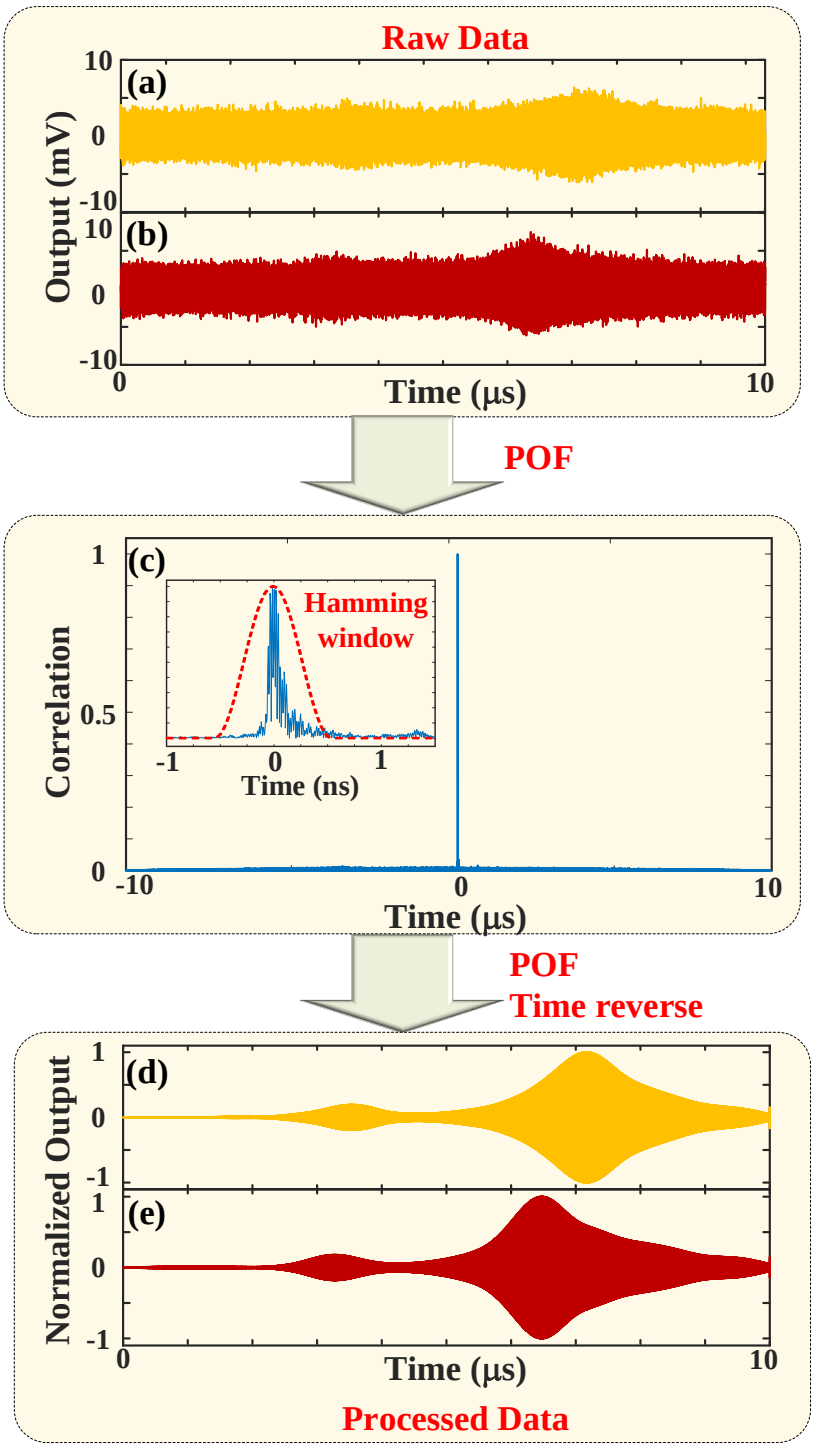

Fig. 4.7 (a) Generated filtered LCMW at 22.82 ℃; (b) generated filtered LCMW at 23.03 ℃; (c) the normalized cross-correlation results. The red dash line in the zoom-in figure is the applied Hamming window; (d) the recovered signal corresponding to the filtered LCMW at 22.82 ℃ shown in (a); (e)the recovered signal corresponding to the filtered LCMW at 23.03 ℃ shown in (b).

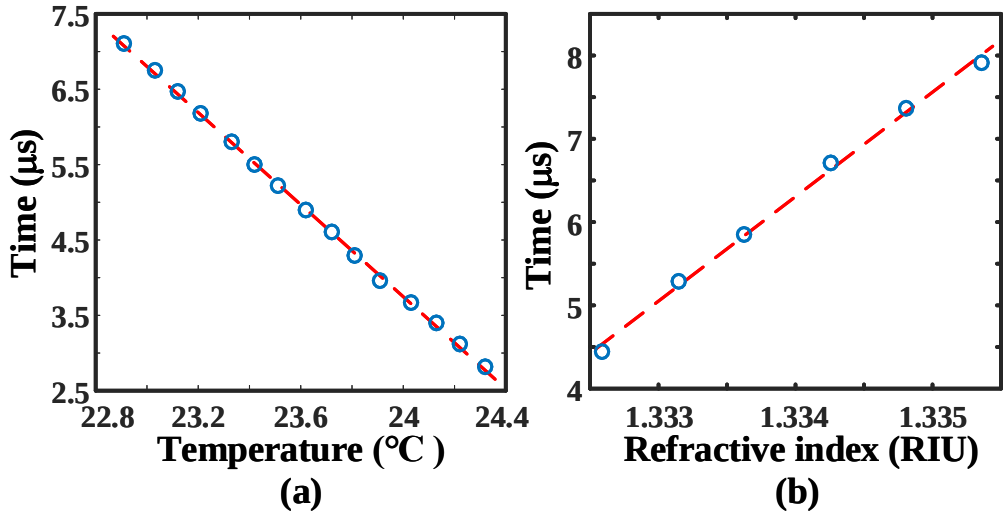

Fig. 4.8 Experimental results. (a) Time locations vs. temperature; (b) time locations vs. refractive index of the cladding. The circles are the experimental data, and the red dash lines show the linear fitting of the experimental data.

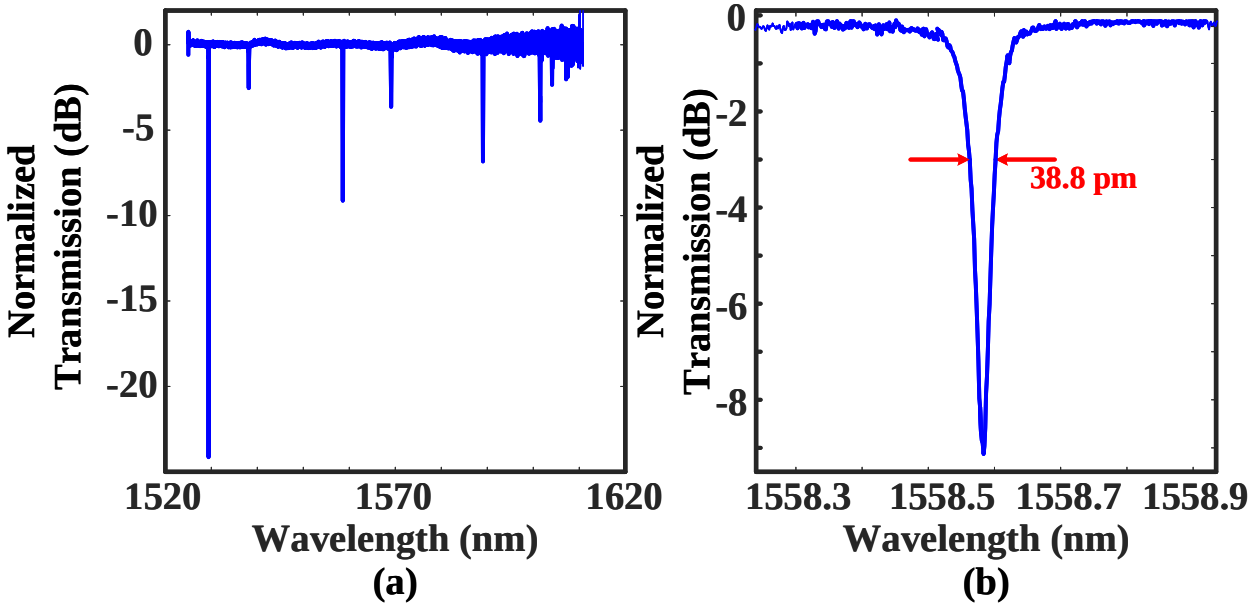

Fig. 4.9 (a) Normalized transmission spectrum of the fabricated microdisk with water cladding; (b) zoom-in view of the TE0 mode resonance of the fabricated microdisk with water cladding.

4.3 Summary

High-speed and high-resolution interrogation of a silicon photonic MDR sensor based on microwave photonic filtering with improved sensing resolution and speed was proposed and experimentally demonstrated. To get a high sensing resolution, a high Q factor MDR by adding a slab waveguide surrounding the waveguide bus and the microdisk was designed and fabricated and its use for temperature and refractive index sensing was performed. To increase interrogation speed, the wavelength change of the MDR was converted to the temporal location change of a microwave waveform, which was generated by filtering a broadband LCMW by an MPF. Since the interrogation can be performed in the electrical domain using a DSP, the speed was significantly increased. To increase interrogation accuracy, the noise of the filtered microwave waveform was removed by a novel algorithm in which two phase-only filtering operations were performed. By using a Hamming window to select the compressed waveform after the first POF, the noise was significantly reduced. The interrogation speed of this system was determined by the temporal duration of the LCMW, which was 10 μs, corresponding an interrogation speed of 100 kHz. The proposed sensor system was experimentally demonstrated. As a temperature sensor, a sensitivity of 76.8 pm/℃ and a resolution of 0.234℃ were achieved. As an refractive index sensor, a sensitivity of 33.28 nm/RIU and a resolution of 1.32×10^{-3} RIU were achieved.

CHAPTER 5 CONCLUSIONS AND FUTURE WORK

5.1 Conclusions

In this thesis, two real-time interrogation systems for a random grating sensor and a MDR sensor were proposed and experimentally demonstrated. By using a high speed oscilloscope to monitor the demodulated sensing information in time domain, high speed and high resolution interrogations were ensured. Furthermore, without any optical interferometer structures, these interrogation systems were ultra stable.

Specifically, in Chapter 2, a background review of FBG sensors and silicon photonic resonator sensors was presented. The advantages and limitations of the previous interrogation systems were discussed.

In Chapter 3, an experimental demonstration of the proposed interrogation system for an HBRG based on WTT mapping was implemented. In the proposed random grating sensor, an ultrashort light pulse form MLL was spectrum sliced by an HBRG to generate two orthogonally polarized spectrums. A LCFBG was used in used in a complementary manner to realise a WTT mapping, and two temporally separated optical pulses were generated with orthogonal polarization. By monitoring the waveform shifts of the two random waveforms using pulse compression technique, the stain and temperature information could be retrieved. Experimental results showed that the proposed interrogation system could provide a stain and temperature resolution better than 7.1 με and 0.79°C at an ultra-high speed of 20 MHz, which could find applications where high speed and high resolution sensing was required.

In Chapter 4, an experimental demonstration of the proposed interrogation system for an MDR sensor based on microwave photonic filtering and WTT mapping was implemented. Because of the instinct feature of integrated optics, silicon photonic resonator sensors enjoyed a high sensitivity for the refractive index changing. In order to get a high detection resolution, a special MDR was designed and fabricated. The MDR was used to implement a microwave photonic bandpass filter with a TLS and PM. By feeding a broadband LCMW to the MPF, a filtered chirped waveform with the central frequency corresponding to the resonant wavelength was obtained. The chirp rate of the LCMW implemented a MTT mapping, and the temporal location of the filtered chirp waveform indicated its central wavelength. By measuring the temporal location of the filtered microwave waveform, the sensing information could be revealed. The experimental results showed that the sensor provided a sensitivity of 76.8 pm/℃ and a resolution of 0.234℃ as a temperature sensor, and a sensitivity of 33.28 nm/RIU and a resolution of 1.32×10^{-3} RIU as an refractive index sensor. The interrogation speed was 100 kHz. Furthermore, the interrogation system provided a wavelength resolution of 1.6×10^{-4} pm at 1550 nm, which was much higher than a commonly used OSA or OVA.

5.2 Future work

Optical sensor technology has been proven to be a powerful tool in numerous applications. In this thesis, two real-time interrogation systems with improved speed and resolution were proposed and demonstrated. The work can be further improved from the following aspects.

1) The limitation of the interrogation resolution of the random grating sensor is the sampling rate of the oscilloscope and the dispersion coefficient of the LCFBG. If a higher sampling rate and a higher dispersion coefficient were available, the sensing sensitivity and the interrogation resolution would be improved.
2) The interrogation speed of the random grating sensor system is determined by the repetition rate of the used MLL. A higher interrogation speed than 20 MHz is achievable by replacing the pulse source with a higher repetition rate. However, the pulse width of the generated pulses limits the maximum repetition rate. In the proposed system, the width of the two output pulses are 20 ns, which promises the highest interrogation speed of 50 MHz.
3) For the MDR sensor, the detection limit depends on the Q factor of the used MDR. The Q factor could be improved by increasing the diameter of the disk. However, the number of existed modes would increase at the same time. A larger MDR sensor could find applications which needs high detection resolution but low dynamic range.
4) The MDR sensor are sensitive to the changing of both temperature and refractive index. A MDR array could be used to discriminate the influence of the temperature changing and the refractive index changing. By setting a MDR reference, the sensing information of temperature and refractive index can be revealed simultaneously.

References

[1] S. Yin, P Ruffin, and F. Yu. *Fiber optic sensors, 2nd ed,* CRC press, 2008.

[2] H. Nakstad and J. T. Kringlebotn, "Oil and gas applications: Probing oil fields," Nat. Photonics, vol. 2, no. 3, pp. 147-149, Mar. 2008.

[3] M. Jones, "Structural-health monitoring: a sensitive issue," Nat. Photonics, vol. 2, no. 3, pp. 153-154, Mar. 2008.

[4] L. Zou, X. Bao, F. Ravet, and L. Chen, "Distributed Brillouin fiber sensor for detecting pipeline buckling in an energy pipe under internal pressure," Appl. Opt., vol. 45, no. 14, pp. 3372-3377, May 2006.

[5] L. Zou, G. A. Ferrier, S. Afshar, Q. Yu, L. Chen, and X. Bao, "Distributed Brillouin scattering sensor for discrimination of wall-thinning defects in steel pipe under internal pressure," Appl. Opt., vol. 43, no. 7, pp. 1583-1588, Mar. 2004.

[6] S.-C. Huang, W.-W. Lin, M.-T. Tsai, and M.-H. Chen, "Fiber optic in-line distributed sensor for detection and localization of the pipeline leaks," Sens. Actuators, A, vol. 135, no. 2, pp. 570-579, Apr. 2007.

[7] O. S. Wolfbeis, "Fiber-optic chemical sensors and biosensors," Anal. Chem., vol. 80, no. 12, pp. 4269-4283, May 2008.

[8] R. Wolthuis, D. McCrae, E. Saaski, J. Hartl, and G. Mitchell, "Development of a medical fiber-optic pH sensor based on optical absorption," IEEE Trans. Biomed. Eng., vol. 39, no. 5, pp. 531-537, May 1992.

[9] R. Wolthius, D. McCrae, J. C. Hartl, E. Saaski, G. L. Mitchell, K. Garcin, and R. Willard, "Development of a medical fiber-optic oxygen sensor based on optical absorption change," IEEE Trans. Biomed. Eng., vol. 39, no. 2, pp. 185-193, Feb. 1992.

[10] P. A. E. Piunno, U. J. Krull, R. H. E. Hudson, M. J. Damha, and H. Cohen, "Fiber optic biosensor for fluorimetric detection of DNA hybridization," Anal. Chim. Acta, vol. 288, no. 3, pp. 205-214, Apr. 1994.

[11] Z. Tian, S. S.-H. Yam, J. Barnes, W. Bock, P. Greig, J. M. Fraser, H.-P. Loock, and R. D. Oleschuk, "Refractive index sensing with Mach--Zehnder interferometer based on concatenating two single-mode fiber tapers," IEEE Photon. Technol. Lett., vol. 20, no. 8, pp. 626-628, Apr. 2008.

[12] Z. Tian, S. H. Yam, and H. P. Loock, “Refractive index sensor based on an abrupt taper Michelson interferometer in a single-mode fiber,” Opt. Lett., vol. 33, no. 10, pp. 1105-1107, May 2008.

[13] B. Huttner, B. Gisin, and N. Gisin, "Distributed PMD measurement with a polarization-OTDR in optical fibers," J. Lightw. Technol., vol. 17, no. 10, p. 1843, Oct. 1999.

[14] M. G. Tanner, S. D. Dyer, B. Baek, R. H. Hadfield, and S. Woo Nam, "High-resolution single-mode fiber-optic distributed Raman sensor for absolute temperature

measurement using superconducting nanowire single-photon detectors," Appl. Phys. Lett., vol. 99, no. 20, p. 201110, Nov. 2011.

[15] M. Niklès, L. Thévenaz, and P. A. Robert, "Simple distributed fiber sensor based on Brillouin gain spectrum analysis," Opt. Lett., vol. 21, no. 10, pp. 758-760, May. 1996.

[16] R. A. Bergh, H. C. Lefevre, and H. J. Shaw, "Compensation of the optical Kerr effect in fiber-optic gyroscopes," Opt. Lett., vol. 7, no. 6, pp. 282-284, Jun. 1982.

[17] A. D. Kersey, T. A. Berkoff, and W. W. Morey, "Multiplexed fiber Bragg grating strain-sensor system with a fiber Fabry--Perot wavelength filter," Opt. Lett., vol. 18, no. 16, pp. 1370-1372, Aug. 1993.

[18] H. J. Patrick, G. M. Williams, A. D. Kersey, J. R. Pedrazzani, and A. M. Vengsarkar, "Hybrid fiber Bragg grating/long period fiber grating sensor for strain/temperature discrimination," IEEE Photon. Technol. Lett., vol. 8, no. 9, pp. 1223-1225, Sept. 1996.

[19] Y. Xu, P. Lu, S. Gao, D. Xiang, S. Mihailov, and X. Bao, "Optical fiber random grating-based multiparameter sensor," Opt. Lett., vol. 40, no. 23, pp. 5514-5517, Dec. 2015.

[20] K. T. V. Grattan and T. Sun, "Fiber optic sensor technology: an overview," Sens. Actuators, A, vol. 82, no. 1-3, pp. 40-61, May 2000.

[21] A. D. Kersey, M. A. Davis, H. J. Patrick, M. LeBlanc, K. P. Koo, C. G. Askins, M. A. Putnam, and E. J. Friebele, "Fiber grating sensors," J. Lightw. Technol., vol. 15, no. 8, pp. 1442-1463, Aug. 1997.

[22] P. Kozma, F. Kehl, E. Ehrentreich-Förster, C. Stamm, and F. F. Bier, "Integrated planar optical waveguide interferometer biosensors: A comparative review," Biosens. Bioelectron., vol. 58, no. 15, pp. 287-307, Aug. 2014.

[23] R. G. Heideman and P. V. Lambeck, "Remote opto-chemical sensing with extreme sensitivity: design, fabrication and performance of a pigtailed integrated optical phase-modulated Mach--Zehnder interferometer system," Sens. Actuators, B, vol. 61, no. 1-3, pp. 100-127, Dec. 1999.

[24] A. Brandenburg, "Differential refractometry by an integrated-optical Young interferometer," Sens. Actuators, B, vol. 39, no. 1-3, pp. 266-271, Mar. 1997.

[25] J. Moros, J. A. Lorenzo, P. Lucena, L. Miguel Tobaria, and J. J. Laserna, "Simultaneous Raman Spectroscopy- Laser-Induced Breakdown Spectroscopy for instant standoff analysis of explosives using a mobile integrated sensor platform," Anal. Chem., vol. 82, no. 4, pp. 1389-1400, Jan. 2010.

[26] B. J. Eggleton, C. G. Poulton, and R. Pant, "Inducing and harnessing stimulated Brillouin scattering in photonic integrated circuits," Adv. Opt. Photonics, vol. 5, no. 4, pp. 536-587, Dec. 2013.

[27] T. Suhara, T. Taniguchi, M. Uemukai, H. Nishihara, T. Hirata, S. Iio, and M. Suehiro, "Monolithic integrated-optic position/displacement sensor using waveguide gratings and QW-DFB laser," IEEE Photon. Technol. Lett., vol. 7, no. 10, pp. 1195-1197, Oct. 1995.

[28] E. Krioukov, D. J. W. Klunder, A. Driessen, J. Greve, and C. Otto, "Sensor based on an integrated optical microcavity," Opt. Lett., vol. 27, no. 7, pp. 512-514, Apr. 2002.

[29] I. Rea, M. Iodice, G. Coppola, I. Rendina, A. Marino, and L. De Stefano, "A porous silicon-based Bragg grating waveguide sensor for chemical monitoring," Sens. Actuators, B, vol. 139, no. 1, pp. 39-43, May 2009.

[30] P. Prabhathan, V. M. Murukeshan, Z. Jing, and P. V. Ramana, "Compact SOI nanowire refractive index sensor using phase shifted Bragg grating," Opt. Express, vol. 17, no. 17, pp. 15330-15341, Aug. 2009.

[31] K. De Vos, I. Bartolozzi, E. Schacht, P. Bienstman, and R. Baets, "Silicon-on-Insulator microring resonator for sensitive and label-free biosensing," Opt. Express, vol. 15, no. 12, pp. 7610-7615, June 2007.

[32] S. M. Grist, S. A. Schmidt, J. Flueckiger, V. Donzella, W. Shi, S. T. Fard, J. T. Kirk, D. M. Ratner, K. C. Cheung, and L. Chrostowski, "Silicon photonic micro-disk resonators for label-free biosensing," Opt. Express, vol. 21, no. 7, pp. 7994-8006, Apr. 2013.

[33] L. Chrostowski, S. M. Grist, J. Flueckiger, W. Shi, X. Wang, E. Ouellet, H. Yun, M. Webb, B. Nie, Z. Liang, and others, "Silicon photonic resonator sensors and devices.," 2012.

[34] C. G. Askins, M. A. Putnam, G. M. Williams, and E. J. Friebele, "Stepped-wavelength optical-fiber Bragg grating arrays fabricated in line on a draw tower," Opt. Lett., vol. 19, no. 2, pp. 147-149, Jan. 1994.

[35] Q. Zhang, D. A. Brown, H. Kung, J. E. Townsend, M. Chen, L. J. Reinhart, and T. F. Morse, "Use of highly overcoupled couplers to detect shifts in Bragg wavelength (strain sensors)," Electron. Lett., vol. 31, no. 6, pp. 480-482, Mar. 1995.

[36] H. Xia, C. Zhang, H. Mu, and D. Sun, "Edge technique for direct detection of strain and temperature based on optical time domain reflectometry," Appl. Opt., vol. 48, no. 2, pp. 189-197, Jan. 2009.

[37] Y. J. Rao, L. Zhang, I. Bennion, and D. A. Jackson, "Dual-cavity interferometric wavelength-shift detection for in-fiber Bragg grating sensors," Opt. Lett., vol. 21, no. 19, pp. 1556-1558, Oct. 1996.

[38] C. Wang and J. Yao, "Ultrafast and ultrahigh-resolution interrogation of a fiber Bragg grating sensor based on interferometric temporal spectroscopy," J. Lightw. Technol., vol. 29, no. 19, pp. 2927-2933, Oct. 2011.

[39] J. Yao, "Photonic generation of microwave arbitrary waveforms," Opt. Commun., vol. 284, no. 15, pp. 3723-3736, Jul. 2011.

[40] Y. Wang, J. Zhang, O. Coutinho, and J. Yao, "Interrogation of a linearly chirped fiber Bragg grating sensor with high resolution using a linearly chirped optical waveform," Opt. Lett., vol. 40, no. 21, pp. 4923-4926, Nov. 2015.

[41] Y. Wang, J. Zhang, and J. Yao, "An optoelectronic oscillator for high sensitivity temperature sensing," IEEE Photon. Technol. Lett., vol. 28, no. 13, pp. 1458-1461, Jul. 2016.

[42] W. Liu, M. Li, C. Wang, and J. Yao, "Real-time interrogation of a linearly chirped fiber Bragg grating sensor based on chirped pulse compression with improved resolution and signal-to-noise ratio," J. Lightw. Technol., vol. 29, no. 9, pp. 1239-1247, May 2011.

[43] O. Xu, J. Zhang, and J. Yao, "High speed and high resolution interrogation of a fiber Bragg grating sensor based on microwave photonic filtering and chirped microwave pulse compression," Opt. Lett., vol. 41, no. 21, pp. 4859-4862, Nov. 2016.

[44] S. X. Chew, X. Yi, W. Yang, C. Wu, L. Li, L. Nguyen, and R. Minasian, "Optoelectronic Oscillator Based Sensor Using an On-Chip Sensing Probe," IEEE Photon. J., vol. 9, no. 2, pp. 1-9, Mar. 2017.

[45] K. O. Hill, Y. Fujii, D. C. Johnson, and B. S. Kawasaki, "Photosensitivity in optical fiber waveguides: Application to reflection filter fabrication," Appl. Phys. Lett., vol. 32, no. 10, pp. 647-649, Aug. 1978.

[46] Y. K. Chen, C. J. Hu, C. C. Lee, K. M. Feng, M. K. Lu, C.-H. Chang, Y. K. Tu, and S. L. Tzeng, "Low-crosstalk and compact optical add-drop multiplexer using a multiport circulator and fiber Bragg gratings," IEEE Photon. Technol. Lett., vol. 12, no. 10, pp. 1394-1396, Oct. 2000.

[47] L. Talaverano, S. Abad, S. Jarabo, and M. Lopez-Amo, "Multiwavelength fiber laser sources with Bragg-grating sensor multiplexing capability," J. Lightw. Technol., vol. 19, no. 4, p. 553, Apr. 2001.

[48] B. Samson, A. Carter, and K. Tankala, "Doped fibres: Rare-earth fibres power up," Nat. Photonics, vol. 5, no. 8, pp. 466-467, Aug 2011.

[49] M. Li, L.-Y. Shao, J. Albert, and J. Yao, "Continuously tunable photonic fractional temporal differentiator based on a tilted fiber Bragg grating," IEEE Photon. Technol. Lett., vol. 23, no. 4, pp. 251-253, Feb. 2011.

[50] K. Zhou, G. Simpson, X. Chen, L. Zhang, and I. Bennion, "High extinction ratio in-fiber polarizers based on 45 tilted fiber Bragg gratings," Opt. Lett., vol. 30, no. 11, pp. 1285-1287, Jun. 2005.

[51] L. Yan, R. A. Barankov, P. Steinvurzel, and S. Ramachandran, "Side-tap modal channel monitor for mode division multiplexed (MDM) systems," in Optical Fiber Communication Conference, 2012.

[52] E. Chehura, S. W. James, and R. P. Tatam, "Temperature and strain discrimination using a single tilted fibre Bragg grating," Opt. Commun., vol. 275, no. 2, pp. 344-347, July 2007.

[53] Y. Miao, B. Liu, W. Zhang, B. Dong, H. Zhou, and Q. Zhao, "Dynamic temperature compensating interrogation technique for strain sensors with tilted fiber Bragg gratings," IEEE Photon. Technol. Lett., vol. 20, no. 16, pp. 1393-1395, Aug. 2008.

[54] Y. X. Jin, C. C. Chan, X. Y. Dong, and Y. F. Zhang, "Temperature-independent bending sensor with tilted fiber Bragg grating interacting with multimode fiber," Opt. Commun., vol. 282, no. 19, pp. 3905-3907, Oct. 2009.

[55] Q. Jiang, D. Hu, and M. Yang, "Simultaneous measurement of liquid level and surrounding refractive index using tilted fiber Bragg grating," Sens. Actuators, A, vol. 170, no. 1-2, pp. 62-65, Nov. 2011.

[56] T. Guo, A. Ivanov, C. Chen, and J. Albert, "Temperature-independent tilted fiber grating vibration sensor based on cladding-core recoupling," Opt. Lett., vol. 33, no. 9, pp. 1004-1006, May 2008.

[57] K. O. Hill and G. Meltz, "Fiber Bragg grating technology fundamentals and overview," J. Lightw. Technol., vol. 15, no. 8, pp. 1263-1276, Aug. 1997.

[58] F. Ouellette, "All-fiber filter for efficient dispersion compensation," Opt. Lett., vol. 16, no. 5, pp. 303-305, Mar. 1991.

[59] T. Komukai, T. Yamamoto, and S. Kawanishi, "Optical pulse generator using phase modulator and linearly chirped fiber Bragg gratings," IEEE Photon. Technol. Lett., vol. 17, no. 8, pp. 1746-1748, Aug. 2005.

[60] J. A. R. Williams, I. Bennion, and L. Zhang, "The compression of optical pulses using self-phase-modulation and linearly chirped Bragg-gratings in fibers," IEEE Photon. Technol. Lett., vol. 7, no. 5, pp. 491-493, May. 1995.

[61] M. Li and J. Yao, "Photonic generation of continuously tunable chirped microwave waveforms based on a temporal interferometer incorporating an optically pumped linearly chirped fiber Bragg grating," IEEE Trans. Microw. Theory Techn., vol. 59, no. 12, pp. 3531-3537, Dec. 2011.

[62] F. Zeng, J. Wang, and J. Yao, "All-optical microwave bandpass filter with negative coefficients based on a phase modulator and linearly chirped fiber Bragg gratings," Opt. Lett., vol. 30, no. 17, pp. 2203-2205, Sep. 2005.

[63] S. Li and T. Chan, "Electrical wavelength-tunable actively mode-locked fiber ring laser with a linearly chirped fiber Bragg grating," IEEE Photon. Technol. Lett., vol. 10, no. 6, pp. 799-801, June 1998.

[64] J. Azaña and L. R. Chen, "Synthesis of temporal optical waveforms by fiber Bragg gratings: a new approach based on space-to-frequency-to-time mapping," JOSA B, vol. 19, no. 11, pp. 2758-2769, Nov. 2002.

[65] G. P. Agrawal and S. Radic, "Phase-shifted fiber Bragg gratings and their application for wavelength demultiplexing," IEEE Photon. Technol. Lett., vol. 6, no. 8, pp. 995-997, Aug. 1994.

[66] N. K. Berger, B. Levit, B. Fischer, M. Kulishov, D. V. Plant, and J. Azaña, "Temporal differentiation of optical signals using a phase-shifted fiber Bragg grating," Opt. Express, vol. 15, no. 2, pp. 371-381, Jan. 2007.

[67] N. Q. Ngo, "Design of an optical temporal integrator based on a phase-shifted fiber Bragg grating in transmission," Opt. Lett., vol. 32, no. 20, pp. 3020-3022, Oct. 2007.

[68] M. H. Asghari and J. Azaña, "All-optical Hilbert transformer based on a single phase-shifted fiber Bragg grating: design and analysis," Opt. Lett., vol. 34, no. 3, pp. 334-336, Feb. 2009.

[69] A. Melloni, M. Chinello, and M. Martinelli, "All-optical switching in phase-shifted fiber Bragg grating," IEEE Photon. Technol. Lett., vol. 12, no. 1, pp. 42-44, Jan. 2000.

[70] W. Li and J. Yao, "A wideband frequency tunable optoelectronic oscillator incorporating a tunable microwave photonic filter based on phase-modulation to intensity-modulation conversion using a phase-shifted fiber Bragg grating," IEEE Trans. Microw. Theory Techn., vol. 60, no. 6, pp. 1735-1742, June 2012.

[71] A. I. Azmi, D. Sen, W. Sheng, J. Canning, and G.-D. Peng, "Performance enhancement of vibration sensing employing multiple phase-shifted fiber Bragg grating," J. Lightw. Technol., vol. 29, no. 22, pp. 3453-3460, Nov. 2011.

[72] Q. Wu and Y. Okabe, "Ultrasonic sensor employing two cascaded phase-shifted fiber Bragg gratings suitable for multiplexing," Opt. Lett., vol. 37, no. 16, pp. 3336-3338, Aug. 2012.

[73] M. I. Zibaii, A. Kazemi, H. Latifi, M. K. Azar, S. M. Hosseini, and M. H. Ghezelaiagh, "Measuring bacterial growth by refractive index tapered fiber optic biosensor," J. Photochem. Photobiol., B, vol. 101, no. 3, pp. 313-320, Dec. 2010.

[74] V. Jayaraman, Z.-M. Chuang, and L. A. Coldren, "Theory, design, and performance of extended tuning range semiconductor lasers with sampled gratings," IEEE J. Quantum Electron., vol. 29, no. 6, pp. 1824-1834, Jun. 1993.

[75] Y. Dai and J. Yao, "Numerical study of a DFB semiconductor laser and laser array with chirped structure based on the equivalent chirp technology," IEEE J. Quantum Electron., vol. 44, no. 10, pp. 938-945, Sep. 2008.

[76] W. Li, X. Zhang, and J. Yao, "Experimental demonstration of a multi-wavelength distributed feedback semiconductor laser array with an equivalent chirped grating profile based on the equivalent chirp technology," Opt. Express, vol. 21, no. 17, pp. 19966-19971, Aug. 2013.

[77] H. Zhu, X. Xu, H. Wang, D. Kong, S. Liang, L. Zhao, and W. Wang, "The fabrication of eight-channel DFB laser array using sampled gratings," IEEE Photon. Technol. Lett., vol. 22, no. 5, pp. 353-355, Mar. 2010.

[78] J. Hubner, D. Zauner, and M. Kristensen, "Strong sampled Bragg gratings for WDM applications," IEEE Photon. Technol. Lett., vol. 10, no. 4, pp. 552-554, Apr. 1998.

[79] X. Shu, K. Chisholm, I. Felmeri, K. Sugden, A. Gillooly, L. Zhang, and I. Bennion, "Highly sensitive transverse load sensing with reversible sampled fiber Bragg gratings," Appl. Phys. Lett., vol. 83, no. 15, pp. 3003-3005, Oct 2003.

[80] A. Sun and Z. Wu, "Multimode interference in single mode--multimode FBG for simultaneous measurement of strain and bending," IEEE Sensors J., vol. 15, no. 6, pp. 3390-3394, Jun. 2015.

[81] C. Gouveia, P. A. S. Jorge, J. M. Baptista, and O. Frazão, "Fabry--Pérot cavity based on a high-birefringent fiber Bragg grating for refractive index and temperature measurement," IEEE Sensors J., vol. 12, no. 1, pp. 17-21, Jan. 2012.

[82] T. Erdogan, "Fiber grating spectra," J. Lightw. Technol., vol. 15, no. 8, pp. 1277-1294, Aug. 1997.

[83] Y.-J. Rao, "Fiber Bragg grating sensors: principles and applications," in Optical fiber sensor technology, Springer, 1998, pp. 355-379.

[84] T. E. Murphy, J. T. Hastings, and H. I. Smith, "Fabrication and characterization of narrow-band Bragg-reflection filters in silicon-on-insulator ridge waveguides," J. Lightw. Technol., vol. 19, no. 12, p. 1938, Dec. 2001.

[85] W. Bogaerts, P. De Heyn, T. Van Vaerenbergh, K. De Vos, S. Kumar Selvaraja, T. Claes, P. Dumon, P. Bienstman, D. Van Thourhout, and R. Baets, "Silicon microring resonators," Laser \& Photonics Reviews, vol. 6, no. 1, pp. 47-73, Sep. 2012.

[86] A. Densmore, D.-X. Xu, P. Waldron, S. Janz, P. Cheben, J. Lapointe, A. Delge, B. Lamontagne, J. H. Schmid, and E. Post, "A silicon-on-insulator photonic wire based evanescent field sensor," IEEE Photon. Technol. Lett., vol. 18, no. 23, pp. 2520-2522, Dec. 2006.

[87] I. M. White and X. Fan, "On the performance quantification of resonant refractive index sensors," Opt. Express, vol. 16, no. 2, pp. 1020-1028, Jan. 2008.

[88] B. E. Little, J. S. Foresi, G. Steinmeyer, E. R. Thoen, S. T. Chu, H. A. Haus, E. P. Ippen, L. C. Kimerling, and W. Greene, "Ultra-compact Si-SiO 2 microring resonator optical channel dropping filters," IEEE Photon. Technol. Lett., vol. 10, no. 4, pp. 549-551, Apr. 1998.

[89] T. Hu, W. Wang, C. Qiu, P. Yu, H. Qiu, Y. Zhao, X. Jiang, and J. Yang, "Thermally tunable filters based on third-order microring resonators for WDM applications," IEEE Photon. Technol. Lett., vol. 24, no. 6, p. 524, Mar. 2012.

[90] J. Cardenas, M. A. Foster, N. Sherwood-Droz, C. B. Poitras, H. L. R. Lira, B. Zhang, A. L. Gaeta, J. B. Khurgin, P. Morton, and M. Lipson, "Wide-bandwidth continuously tunable optical delay line using silicon microring resonators," Opt. Express, vol. 18, no. 25, pp. 26525-26534, Dec. 2010.

[91] T. Claes, W. Bogaerts, and P. Bienstman, "Experimental characterization of a silicon photonic biosensor consisting of two cascaded ring resonators based on the Vernier-effect and introduction of a curve fitting method for an improved detection limit," Opt. Express, vol. 18, no. 22, pp. 22747-22761, Oct. 2010.

[92] C. T. DeRose, M. R. Watts, D. C. Trotter, D. L. Luck, G. N. Nielson, and R. W. Young, "Silicon microring modulator with integrated heater and temperature sensor for thermal control," in Conference on Lasers and Electro-optics, 2010.

[93] W. J. Westerveld, J. Pozo, P. M. Muilwijk, S. M. Leinders, P. J. Harmsma, E. Tabak, T. C. Dool, K. W. A. Dongen, M. Yousefi, and H. P. Urbach, "Characterization of optical strain sensors based on silicon waveguides," in The European Conference on Lasers and Electro-Optics, 2013.

[94] S. M. Leinders, W. J. Westerveld, J. Pozo, P. Van Neer, B. Snyder, P. O'Brien, H. P. Urbach, N. Jong, and M. D. Verweij, "A sensitive optical micro-machined ultrasound sensor (OMUS) based on a silicon photonic ring resonator on an acoustical membrane," Sci. Rep., vol. 5, p. 14328, Sep. 2015.

[95] T. Claes, J. G. Molera, K. De Vos, E. Schacht, R. Baets, and P. Bienstman, "Label-free biosensing with a slot-waveguide-based ring resonator in silicon on insulator," IEEE Photon. J., vol. 1, no. 3, pp. 197-204, Sep. 2009.

[96] C. A. Barrios, "Analysis and modeling of a silicon nitride slot-waveguide microring resonator biochemical sensor," in SPIE Europe Optics+ Optoelectronics, Prague, 2009.

[97] X. Wang, W. Shi, R. Vafaei, N. A. F. Jaeger, and L. Chrostowski, "Uniform and sampled Bragg gratings in SOI strip waveguides with sidewall corrugations," IEEE Photon. Technol. Lett., vol. 23, no. 5, pp. 290-292, Mar. 2011.

[98] A. Irace, G. Breglio, and A. Cutolo, "All-silicon optoelectronic modulator with 1 GHz switching capability," Electron. Lett., vol. 39, no. 2, pp. 232-233, Jan. 2003.

[99] M. Burla, L. R. Cortés, M. Li, X. Wang, L. Chrostowski, and J. Azaña, "Integrated waveguide Bragg gratings for microwave photonics signal processing," Opt. Express, vol. 21, no. 21, pp. 25120-25147, Oct. 2013.

[100] N. N. Klimov, S. Mittal, M. Berger, and Z. Ahmed, "On-chip silicon waveguide Bragg grating photonic temperature sensor," Opt. Lett., vol. 40, no. 17, pp. 3934-3936, Sep. 2015.

[101] M. Borselli, T. J. Johnson, and O. Painter, "Beyond the Rayleigh scattering limit in high-Q silicon microdisks: theory and experiment," Opt. Express, vol. 13, no. 5, pp. 1515-1530, Mar. 2005.

[102] M. R. Watts, D. C. Trotter, R. W. Young, and A. L. Lentine, "Ultralow power silicon microdisk modulators and switches," in Group IV Photonics, 2008 5th IEEE International Conference on, 2008.

[103] V. Passaro, C. d. Tullio, B. Troia, M. L. Notte, G. Giannoccaro, and F. D. Leonardis, "Recent advances in integrated photonic sensors," Sensors, vol. 12, no. 11, pp. 15558-15598, Nov. 2012.

[104] G.-D. Kim, H.-S. Lee, C.-H. Park, S.-S. Lee, B. T. Lim, H. K. Bae, and W.-G. Lee, "Silicon photonic temperature sensor employing a ring resonator manufactured using a standard CMOS process," Opt. Express, vol. 18, no. 21, pp. 22215-22221, Oct. 2010.

[105] S. M. Melle, K. Liu, and R. M. Measures, "A passive wavelength demodulation system for guided-wave Bragg grating sensors," IEEE Photon. Technol. Lett., vol. 4, no. 5, pp. 516-518, May 1992.

[106] S. M. Melle, A. T. Alavie, S. Karr, T. Coroy, K. Liu, and R. M. Measures, "A Bragg grating-tuned fiber laser strain sensor system," IEEE Photon. Technol. Lett., vol. 5, no. 2, pp. 263-266, Feb. 1993.

[107] A. D. Kersey, T. A. Berkoff, and W. W. Morey, "High-resolution fibre-grating based strain sensor with interferometric wavelength-shift detection," Electron. Lett., vol. 28, no. 3, pp. 236-238, Jan. 1992.

[108] K. P. Koo and A. D. Kersey, "Fibre laser sensor with ultrahigh strain resolution using interferometric interrogation," Electron. Lett., vol. 31, no. 14, pp. 1180-1182, Jul. 1995.

[109] M. D. Todd, G. A. Johnson, and B. L. Althouse, "A novel Bragg grating sensor interrogation system utilizing a scanning filter, a Mach-Zehnder interferometer and a 3× 3 coupler," Meas. Sci. Technol., vol. 12, no. 7, p. 771, Jul. 2001.

[110] J. Yao, "Photonics to the rescue: A fresh look at microwave photonic filters," IEEE Microw. Mag., vol. 16, no. 8, pp. 46-60, Sep. 2015.

[111] W. Li, M. Li, and J. Yao, "A narrow-passband and frequency-tunable microwave photonic filter based on phase-modulation to intensity-modulation conversion using a phase-shifted fiber Bragg grating," IEEE Trans. Microw. Theory Techn., vol. 60, no. 5, pp. 1287-1296, May 2012.

[112] J. Yao, "Optoelectronic Oscillators for High Speed and High Resolution Optical Sensing," J. Lightw. Technol., vol. 35, no. 16, pp. 3489-3497, Aug. 2017.

[113] M. Li, W. Li, J. Yao, and J. Azaña, "Femtometer-resolution wavelength interrogation using an optoelectronic oscillator," in Photonics Conference (IPC), 2012 IEEE, 2012.

[114] H. Y. Fu, H. L. Liu, X. Dong, H. Y. Tam, P. K. A. Wai, and C. Lu, "High-speed fibre Bragg grating sensor interrogation using dispersion compensation fibre," Electron. Lett., vol. 44, no. 10, pp. 618-619, May 2008.

[115] E. J. Ahmad, C. Wang, D. Feng, Z. Yan, and L. Zhang, "High Temporal and Spatial Resolution Distributed Fiber Bragg Grating Sensors Using Time-Stretch Frequency-Domain Reflectometry," J. Lightw. Technol., vol. 35, no. 16, pp. 3289-3295, Aug. 2017.

Publications

Journal Papers:

[1] H. Deng, J. Zhang, X. Chen, and J. P. Yao, "Photonic generation of a phase-coded chirp microwave waveform with increased TBWP," IEEE Photon. Technol. Lett., vol. 19, no. 17, pp. 1420-1423, Sep. 2017.

[2] O. Xu, J. Zhang, H. Deng, and J. P. Yao, "Dual-frequency optoelectronic oscillator for temperature-insensitive interrogation of a FBG sensor," IEEE Photon. Technol. Lett., vol. 29, no. 4, pp. 357-360, Feb. 2017.

[3] H. Deng, P. Lu, S. Mihailov, and J. P. Yao, "High-speed and high-resolution interrogation of a strain and temperature random grating sensor," Opt. Lett., submitted.

[4] H. Deng, W. Zhang, and J. P. Yao, "High-speed and high-resolution interrogation of a silicon photonic microdisk sensor based on microwave photonic filtering," IEEE/OSA J. Lightw. Technol., submitted.

Conference Papers:

[1] H. Deng, J. Zhang, X. Chen, and J. P. Yao, "Photonic generation of a phase-coded chirp microwave waveform with an Increased TBWP," Photonics North 2017, 6-8 June, Ottawa, ON, Canada.

[2] H. Deng and J. P. Yao, "High-speed and high-resolution interrogation of a fiber Bragg grating temperature sensor," Photonics North 2017, 6-8 June, Ottawa, ON, Canada.

[3] H. Deng, P. Lu, S. Mihailov, and J. P. Yao, “Photonic generation of pseudo random microwave waveform based on a random fiber grating,” OFC2018, March 2018, San Diego, California, USA.